PHYSICAL REVIEW D **86,** 075010 (2012)

Constrained MSSM favoring new territories: The impact of new LHC limits and a 125 GeV Higgs boson

Andrew Fowlie,[1,*] Malgorzata Kazana,[2,†] Kamila Kowalska,[2,‡] Shoaib Munir,[2,§] Leszek Roszkowski,[2,‖]
Enrico Maria Sessolo,[2,¶] Sebastian Trojanowski,[2,**] and Yue-Lin Sming Tsai[2,††]

(The BayesFITS Group)

[1]*Department of Physics and Astronomy, University of Sheffield, Sheffield S3 7RH, United Kingdom*
[2]*National Centre for Nuclear Research, Hoża 69, 00-681 Warsaw, Poland*
(Received 21 June 2012; published 8 October 2012)

We present an updated and extended global analysis of the constrained MSSM (CMSSM) taking into account new limits on supersymmetry from ~5/fb data sets at the LHC. In particular, in the case of the razor limit obtained by the CMS Collaboration we simulate detector efficiency for the experimental analysis and derive an approximate but accurate likelihood function. We discuss the impact on the global fit of a possible Higgs boson with mass near 125 GeV, as implied by recent data, and of a new improved limit on $\mathrm{BR}(B_s \to \mu^+\mu^-)$. We identify high posterior probability regions of the CMSSM parameters as the stau-coannihilation and the A-funnel region, with the importance of the latter now being much larger due to the combined effect of the above three LHC results and of dark matter relic density. We also find that the focus point region is now disfavored. Ensuing implications for superpartner masses favor even larger values than before, and even lower ranges for dark matter spin-independent cross section, $\sigma_p^{\mathrm{SI}} \lesssim 10^{-9}$ pb. We also find that relatively minor variations in applying experimental constraints can induce a large shift in the location of the best-fit point. This puts into question the robustness of applying the usual χ^2 approach to the CMSSM. We discuss the goodness-of-fit and find that, while it is difficult to calculate a p-value, the $(g-2)_\mu$ constraint makes, nevertheless, the overall fit of the CMSSM poor. We consider a scan without this constraint, and we allow μ to be either positive or negative. We find that the global fit improves enormously for both signs of μ, with a slight preference for $\mu < 0$ caused by a better fit to $\mathrm{BR}(b \to s\gamma)$ and $\mathrm{BR}(B_s \to \mu^+\mu^-)$.

DOI: 10.1103/PhysRevD.86.075010 PACS numbers: 12.60.Jv

I. INTRODUCTION

The experimental collaborations ATLAS and CMS at the Large Hadron Collider (LHC) have each so far collected around 5/fb of data and have analyzed a large part of it to set new improved limits on several models of new physics beyond the Standard Model (SM), including low-energy supersymmetry (SUSY). In particular, lower limits on the soft masses m_0 and $m_{1/2}$ of the constrained Minimal Supersymmetric Standard Model (CMSSM) [1] have been pushed further up by a recent CMS analysis of all-hadronic final states, which applied a razor method to 4.4/fb of data [2]. (In contrast, the other two free parameters of the CMSSM, A_0 and $\tan\beta$ remain almost unaffected by the above data). This result considerably improved previous limits by the same collaboration using the same method with 0.8/fb of data [3], as well as limits from the α_T method using 1.1/fb of data [4] and the large missing transverse momentum method (MHT) with the same data set [5]. Much improved lower limits on SUSY masses have also recently been produced by ATLAS, the strongest of which have been obtained from searches with all-hadronic final states [6,7]. In particular, the recent *0-lepton* search with 2-to-6 jets has resulted in a 95% confidence level (CL) exclusion contour in the CMSSM parameter space with 4.7/fb [6] of data which competes with the razor result in the same region of parameter space.

Furthermore, last year both ATLAS and CMS excluded all but two small windows of SM (and SM-like) Higgs mass range, by combining their searches in the $\gamma\gamma$, bb, $\tau\tau$, WW and ZZ final states [8,9]. In December 2011 both collaborations also reported some excess of events in the subdominant but background-clean $\gamma\gamma$ final state [10,11]. In the $ZZ \to 4l$ final state a small excess has also been found but at a somewhat smaller mass of around 119 GeV [12,13]. The Tevatron collaborations CDF and D0 also

---

[*] A.Fowlie@sheffield.ac.uk
[†] Malgorzata.Kazana@fuw.edu.pl
[‡] Kamila.Kowalska@fuw.edu.pl
[§] Shoaib.Munir@fuw.edu.pl
[‖] L.Roszkowski@sheffield.ac.uk; On leave of absence from the University of Sheffield.
[¶] Enrico-Maria.Sessolo@fuw.edu.pl
[**] Sebastian.Trojanowski@fuw.edu.pl
[††] Sming.Tsai@fuw.edu.pl

found some excess over a broader mass range [14]. The hints of a possible Higgs signal around 125 GeV generated much excitement and activity [15–20].[1]

Another recent important highlight of experimental progress in constraining SUSY and other frameworks of new physics has been the new, much improved limit $\mathrm{BR}(B_s \to \mu^+\mu^-) < 4.5 \times 10^{-9}$ (95% CL) [23], which is already approaching the SM value of $(3.2 \pm 0.2) \times 10^{-9}$ [24]. Its effect on the CMSSM will also be considerable, as we shall see below.

In a previous paper [25] by the BayesFITS group a global statistical analysis of the CMSSM based on about $1.1/\mathrm{fb}$ of data was presented. In addition to the usual set of relevant constraints from the relic abundance of cold dark matter (DM) in the Universe, direct mass limits from LEP and the Tevatron, flavor physics, etc., one of the most restrictive limits, from the α_T analysis of CMS [4] was applied. The analysis included some crucial features. We generated approximate efficiency and likelihood maps in order to reproduce the CMS α_T limit, as described in detail in Ref. [25]. This allowed us to include the CMS exclusion limit into the combined likelihood function along with the other constraints, and to map out high probability regions of the CMSSM parameter space. Furthermore, in Ref. [26] the impact of recent limits from FermiLAT on dwarf spheroidal galaxies was investigated in order to derive implications of direct and indirect detection of cold DM for the CMSSM, along with an extension of the approximate likelihood maps for the CMS α_T result to significantly larger CMSSM mass parameter ranges, and an update on a number of our results from Ref. [25].

One of the conclusions derived from previous global analyses, both ours and the ones performed by other groups [15,26,27], was that the dominant contribution to the total χ^2 comes from the anomalous magnetic moment of the muon $(g-2)_\mu$. It seems obvious that relaxing this particular constraint would in a natural way improve the CMSSM fit because satisfying it requires quite low masses of the scalars.

In fact, there exists a quite convincing argument to do so. It has been known for years that a significant discrepancy is observed between the experimental measurement of the muon anomalous magnetic moment, coming from the experiment E821 at Brookhaven National Laboratory [28], and its theoretical predictions within the SM framework. The discrepancy is at more than 3σ, $\delta(g-2)_\mu = 28.7 \pm 8.0 \times 10^{-10}$ [29], and is usually interpreted as a strong indication of new physics beyond the SM.

However, since the poor fit of the CMSSM is to such a large extent a result of basically only one constraint, it is worth examining whether it is as robust as the other most important constraints. In fact, despite much effort, there seem to remain a number of issues of which we only highlight a few here. The accuracy of theoretical predictions is strongly affected by the nonperturbative effects related to the low-energy strong interactions. The main leading-order contribution to $\delta(g-2)_\mu$ comes from the hadron vacuum polarization and is between 5×10^{-10} and 6×10^{-10}. It can be related to the measured hadronic cross section provided by the experiment and has been calculated very precisely with a fractional accuracy of 0.7% [29–31]. On the other hand, a next-to-leading order (NLO) contribution of the order of $O(\alpha^3)$ that comes from the light-by-light scattering through the hadronic vacuum, though one order of magnitude smaller than the leading-order (LO) contribution, is much more poorly known (with a fractional accuracy of 30%), since it cannot be calculated accurately based on the experimental data and is strongly model dependent. As a consequence, its contribution to $\delta(g-2)_\mu^{\mathrm{SUSY}}$ is between 2.5×10^{-10} and 4×10^{-10} [32]. Due to all those uncertainties one should be careful in interpreting the effect of $\delta(g-2)_\mu$ on the searches for SUSY, in particular the CMSSM. We, therefore, also present here some global fits both in the presence and in the absence of the $(g-2)_\mu$ constraint.

Relaxing the $(g-2)_\mu$ constraint has an important consequence. Since the supersymmetric contribution to $\delta(g-2)_\mu$ is proportional to $\mathrm{sgn}\,\mu$, in order to satisfy the experimental limit one is forced to choose $\mu > 0$, as has been the case in most of the previous global fit analyses. However, with the $(g-2)_\mu$ constraint abandoned, the justification to limit the Higgs/Higgsino mass parameter μ to positive values is no longer there, since the other constraints are much less affected by the sign of μ. The analysis of the impact of the negative μ on the global CMSSM fit was performed in, e.g., Refs. [33,34] for the data from the pre-LHC experiments, but with the $(g-2)_\mu$ constraint taken into account.

On the other hand, for negative μ the fit to $\mathrm{BR}(b \to s\gamma)$ actually improves considerably [34] in the higher superpartner mass ranges implied by new LHC limits. This is because, in order to provide a contribution from SUSY to the positive discrepancy between the experimental and the SM values, one actually needs positive contributions from both the charged Higgs/top and the chargino/stop loops, the latter of which is inverse-proportional to the sign of μ. As we shall see, considering both signs of μ and relaxing the $(g-2)_\mu$ constraint will lead to a rather complex picture. In particular, it will significantly improve the statistical fit of the CMSSM.

In this paper we update our recent global analysis of the CMSSM [25]. While we mainly focus on a Bayesian approach and derive posterior probability density function

---

[1] On July 4th, 2012, the discovery at 4.9σ by CMS [21] and at 5.0σ by ATLAS [22] of a boson consistent with the SM Higgs, with mass near 125 GeV, was announced. Particularly, the mass claimed by CMS, 125.3 ± 0.6 GeV, is very close in central value and experimental error to the signal case considered in this paper. In light of this important discovery we shall discuss only the case of a SM-like Higgs boson with mass of 125 GeV.

(pdf) maps, we also compute, for each case we consider, the lowest χ^2 (best-fit point).

We find that it can often be difficult to robustly establish the location of the best-fit point in the CMSSM parameter space, in particular in the most studied case with $\mu > 0$ and the $(g-2)_\mu$ constraint included. Basically, one can find a very good fit in either a (relatively small) stau coannihilation (henceforth $\tilde{\tau}$-coannihilation) region or in a (much more extended) A-funnel region, where A is the pseudoscalar Higgs, both at large $m_{1/2}$ and not as large m_0. First, the lowest values of χ^2 in both regions is often very similar. Second, in the A-funnel region we find an extended *plateau* of comparable, low values of χ^2. As a result, fairly small changes in the treatment of experimental constraints (most notably the LHC lower mass limits via a likelihood function), etc., may cause a large shift in the location of the best-fit point, as we will present in detail below. Our analysis here confirms our earlier assertion spelled out in Ref. [25] (page 17) and puts into question the robustness of results obtained with the χ^2 approach in the framework of the CMSSM.

The main new elements of this study are as follows:

(i) the derivation of an approximate but accurate likelihood map corresponding to the CMS razor limit based on 4.4/fb of data;

(ii) studying the impact of a SM-like Higgs with the mass around 125 GeV;

(iii) considering the effect of the recently updated limit on $\mathrm{BR}(\mathrm{B_s} \to \mu^+\mu^-)$.

All these three ingredients will play a major role in shifting high posterior probability regions from the previously favored $\tilde{\tau}$-coannihilation region, and to some degree also focus point region, to mainly the A-funnel region. In particular, as we discuss below, different ways of mimicking the CMS limit in the likelihood map can have a major impact on both the location and also the value of the best-fit point.

Also, motivated by the results of the previous scans and some theoretical arguments, we move here beyond the usual CMSSM global fit analysis and investigate the effects due to:

(i) relaxing the $(g-2)_\mu$ constraint; and

(ii) taking a negative sign of parameter μ.

This paper is organized as follows. In Sec. II we detail our methodology, including our statistical analysis, scanning algorithm and our treatment of the likelihood from the CMS razor 4.4/fb analysis. In Sec. III we present the results from our scans and discuss their novel features. In Sec. IV we give a statistical discussion of our results and we summarize our findings in Sec. V.

II. METHOD

A. The framework

Our aim is to map out the regions of the parameter space of the SUSY model under consideration that are in best agreement with all relevant experimental constraints. To this end, we follow the strategy outlined in Refs. [25,34]. Here we merely summarize its main features.

In Bayesian statistics, for a theory described by some parameters m, experimental observables $\xi(m)$ can be compared with data d and a posterior probability density function (pdf) $p(m|d)$ can be calculated through Bayes' Theorem

$$p(m|d) = \frac{p(d|\xi(m))\pi(m)}{p(d)}, \tag{1}$$

where the likelihood $p(d|\xi(m)) \equiv \mathcal{L}$ gives the probability density for obtaining d from a measurement of ξ, the prior $\pi(m)$ parametrizes assumptions about the theory prior to performing the measurement and the evidence $p(d) \equiv \mathcal{Z}$ represents the assumptions on the data. As long as one considers only one model the evidence is a constant in the theory parameters, and thus a normalization factor, but, as we will see in Sec. IV B, it is a necessary element of model comparison.

The Bayesian approach yields a simple and natural procedure for calculating the posterior pdf of any limited subset of r variables in the n-dimensional parameter space, $s_{i=1,\ldots,r} \subset m$. One just needs to marginalize, or integrate, over the remaining parameters

$$p(s_{i=1,\ldots,r}|d) = \int p(m|d)d^{n-r}m. \tag{2}$$

To describe our methodology for the Bayesian scan we use the same notation as in Ref. [25].

The likelihood function is a central object in our statistical analysis. We construct it using the prescription described in Ref. [34]. In particular, we model positive measurements with a Gaussian function, and smear out the experimental limits from negative searches using the theoretical error τ.

As stated in the Introduction, in the current analysis we include three new important ingredients provided by LHC data. First, we include the new exclusion limit on the $(m_0, m_{1/2})$ plane of the CMSSM, which has been obtained by the CMS Collaboration by applying the razor method to 4.4/fb of data (see subsection II B for details). Second, we consider the impact of the new information from the Higgs boson experimental searches and we assume a SM-like Higgs with the mass 125 GeV. Finally, we include in the likelihood function the new, improved limit on $\mathrm{BR}(\mathrm{B_s} \to \mu^+\mu^-)$.

B. The efficiency and likelihood maps for the CMS razor 4.4/fb analysis

We derive our LHC likelihood for the CMS search [2,35] for R-parity conserving SUSY in all-hadronic events performed with the razor method summarized below. The results based on the LHC data sample of 4.4/fb of integrated luminosity recorded at $\sqrt{s} = 7$ TeV shows no excess of events over the SM predictions. Our aim is to translate the analysis scheme into a simplified approach to obtain a signal selection efficiency for a large number of points in the CMSSM parameter space.

Studies by the LHC collaborations have shown that jets plus missing energy constraints are relatively insensitive to the values of $\tan\beta$ and A_0 [36], because these parameters have little effect on the squark and gluino masses. The choice of $\tan\beta$ is dictated by the requirement of the appropriate radiative electroweak symmetry breaking (REWSB). The range of the theoretically excluded region in the $(m_0, m_{1/2})$ plane where μ^2 becomes negative and, consequently, REWSB does not occur, strongly depends on the values of $\tan\beta$. We choose a value of $\tan\beta = 3$ which assures that the no-REWSB region does not appear within the analyzed parameter range, and we fix $A_0 = 0$ and $\mu = +1$ (or -1).

For m_0 in the range of 100–4000 GeV and $m_{1/2}$ in the range of 100–2000 GeV we generate a 2-dimensional grid of points in the $(m_0, m_{1/2})$ plane. A scanning step of 50 GeV is chosen in both dimensions. For each point, we generate a mass spectrum and a decay table of supersymmetric particles, using the publicly available packages SOFTSUSY [37] and SUSY-HIT [38], respectively. The mass spectrum and the decay tables are then passed to PYTHIA 6.4 [39] for the event generation process. The hadronized events are then passed to the fast detector simulator PGS4 [40], which reconstructs the physical objects (photons, electrons, muons, hadronically decaying taus, and hadronic jets). We updated the detector parameter-card following the recommendations of the experimental collaboration on the CMS settings.

Our razor analysis performed in this paper follows closely the one of the CMS Collaboration [2]. All reconstructed events are divided into six disjoint event samples (boxes), dependent on the presence or absence of a lepton of a given flavor: electron box, muon box, three dilepton boxes, and hadronic box. For the analysis described in this paper we limit ourselves to reconstructing the hadronic box, which has been shown to yield an excellent approximation of the overall bound with 4.4/fb [2].

At the preselection stage cuts are applied on the transverse energies E_T and the pseudorapidities η of the reconstructed jets: $E_T > 40$ GeV, $|\eta| < 3$ for all jets, and $E_T > 60$ GeV for two leading jets. All jets appearing in a single event are grouped together to form two megajets, which we label jet_1 and jet_2. The selection of the preferred jet combination is based on the invariant mass of the dijet system. All possible combinations of jets are taken into account and the one is chosen for which the invariant mass is minimal.

A pair of megajets should reconstruct the energy distribution of the visible decay products in the center of mass (CM) frame. However, due to the presence of two unseen lightest SUSY particles (LSP), it is possible to reconstruct this frame only approximately. The idea of the razor analysis is to replace the CM frame with the so called R-frame, defined as a longitudinally boosted frame in which the energies of the visible products can be written in terms of some Lorentz invariant scale, which correctly approximates the energy distribution in the CM frame. The Lorentz boost factor of the transformation between the CM and R frames is given by

$$\beta_R = \frac{p_z^{\mathrm{jet}_1} + p_z^{\mathrm{jet}_2}}{E^{\mathrm{jet}_1} + E^{\mathrm{jet}_2}} \tag{3}$$

and the longitudinal boost invariant mass scale M_R is defined as

$$M_R = \sqrt{(E^{\mathrm{jet}_1} + E^{\mathrm{jet}_2})^2 - (p_z^{\mathrm{jet}_1} + p_z^{\mathrm{jet}_2})^2}. \tag{4}$$

With such a definition, M_R approximates the peak in the energy distribution of the visible decay products. One also defines the transverse mass M_T^R as

$$M_T^R = \sqrt{\frac{E_T^{\mathrm{miss}}(p_T^{\mathrm{jet}_1} + p_T^{\mathrm{jet}_2}) - \vec{E}_T^{\mathrm{miss}} \cdot (\vec{p}_T^{\,\mathrm{jet}_1} + \vec{p}_T^{\,\mathrm{jet}_2})}{2}}, \tag{5}$$

as well as the razor dimensionless ratio,

$$R = \frac{M_T^R}{M_R}. \tag{6}$$

The variable R would peak around zero for the QCD multijets and around 0.5 for the SUSY signal, constituting a good discriminator allowing to reduce the magnitude of the QCD background. The events in the hadronic box are required to satisfy the conditions: $M_R > 400$ GeV and $0.18 < R^2 < 0.5$.

To construct a 2-dimensional pdf for the signal, all accepted events are divided into 38 separate bins in the (M_R, R^2) plane. The corresponding numbers of the observed events (o), expected background events (b) and errors on the expected background yield (δb) are given in Table I [41]. Note that two bins, namely 1200 GeV $< M_R <$ 1600 GeV, $0.3 < R^2 < 0.4$ and 1200 GeV $< M_R <$ 1600 GeV, $0.4 < R^2 < 0.5$, feature a bigger than 3σ excess of the observed signal over the expected background. We will come back to this issue while discussing the probability distribution assigned to each bin.

The efficiency ϵ of the detector is defined as the fraction of events that passed all the cuts. The signal for the ith bin is then computed in the usual way,

$$s_i = \epsilon_i \times \sigma \times \int L, \tag{7}$$

where $\int L$ is an integrated luminosity, here $\int L = 4.4/\mathrm{fb}$, and σ is the total cross section for the production of supersymmetric particles at $\sqrt{s} = 7$ TeV. The probability of observing o_i events in the ith bin, given the known

TABLE I. Bins used in the razor analysis with the corresponding numbers of observed (o) and expected background events ($b \pm \delta b$).

M_R, R^2	500–550, 0.3–0.4	500–550, 0.4–0.5	550–600, 0.3–0.4	550–600, 0.4–0.5	600–650, 0.3–0.4
Observed	246	112	124	85	86
Background	259.5 ± 19.4	118.9 ± 14.4	162.8 ± 16.1	73.6 ± 12.0	104.8 ± 14.8
M_R, R^2	600–650, 0.4–0.5	650–700, 0.2–0.3	650–700, 0.3–0.4	650–700, 0.4–0.5	700–800, 0.2–0.3
Observed	26	192	57	23	247
Background	43.0 ± 9.2	209.8 ± 21.2	68.0 ± 11.6	26.0 ± 7.2	233.9 ± 27.2
M_R, R^2	700–800, 0.3–0.4	700–800, 0.4–0.5	800–900, 0.2–0.3	800–900, 0.3–0.4	800–900, 0.4–0.5
Observed	65	27	92	24	6
Background	74.1 ± 15.1	24.8 ± 8.2	104.3 ± 17.7	29.3 ± 9.4	8.5 ± 4.3
M_R, R^2	900–1000, 0.2–0.3	900–1000, 0.3–0.4	900–1000, 0.4–0.5	1000–1200, 0.18–0.2	1000–1200, 0.2–0.3
Observed	50	13	3	20	31
Background	48.6 ± 12.6	11.3 ± 5.6	2.7 ± 2.2	15.8 ± 5.8	33.1 ± 10.2
M_R, R^2	1000–1200, 0.3–0.4	1000–1200, 0.4–0.5	1200–1600, 0.18–0.2	1200–1600, 0.2–0.3	1200–1600, 0.3–0.4
Observed	5	3	10	13	8
Background	6.3 ± 3.8	1.3 ± 1.3	4.8 ± 2.9	9.3 ± 4.9	1.2 ± 1.2
M_R, R^2	1200–1600, 0.4–0.5	1600–2000, 0.18–0.2	1600–2000, 0.2–0.3	1600–2000, 0.3–0.4	1600–2000, 0.4–0.5
Observed	3	0	0	1	0
Background	0.4 ± 0.4	0.5 ± 0.5	0.6 ± 0.6	0.4 ± 0.4	0.3 ± 0.3
M_R, R^2	2000–2800, 0.18–0.2	2000–2800, 0.2–0.3	2000–2800, 0.3–0.4	2000–2800, 0.4–0.5	2800–3500, 0.18–0.2
Observed	0	0	0	0	0
Background	0.4 ± 0.4	0.4 ± 0.4	0.3 ± 0.3	0.3 ± 0.3	0.3 ± 0.3
M_R, R^2	2800–3500, 0.2–0.3	2800–3500, 0.3–0.4	2800–3500, 0.4–0.5		
Observed	0	0	0		
Background	0.3 ± 0.3	0.3 ± 0.3	0.3 ± 0.3		

number of the expected events s_i, and the number of the expected SM background events b_i, is given by a counting-experiment likelihood (Poisson distribution) convolved with an additional function that takes care of the predicted error on the background yields (δb_i)

$$\mathcal{L}_i(o_i, s_i, b_i) = \int P(o_i|s_i, \bar{b}_i) F(\bar{b}_i|b_i, \delta b_i) d\bar{b}_i, \qquad (8)$$

where

$$P(o_i|s_i, b_i) = \frac{e^{-(s_i+b_i)}(s_i + b_i)^{o_i}}{o_i!}. \qquad (9)$$

The values for o_i, b_i and δb_i are given in Table I. For the bins where the number of the observed events does not exceed the predicted background by more than 3σ (in fact, in our case it never exceeds 2σ), we use for the function F a standard Gaussian distribution

$$F(\bar{b}_i|b_i, \delta b_i) = \frac{1}{\delta b_i \cdot \sqrt{2\pi}} \exp\left[-\frac{1}{2}\left(\frac{\bar{b}_i - b_i}{\delta b_i}\right)^2\right]. \qquad (10)$$

On the other hand, one should be a bit more careful when dealing with the two bins in which the excess of events over the predicted background is more than 3σ. The Poisson distribution (9) peaks at $o_i \approx s_i + (b_i \pm \delta b_i)$. If the number of the observed events in a given bin is not much bigger than the predicted background yield, the maximal likelihood one can obtain in that bin will correspond to the background-only hypothesis (with $s_i = 0$). Any nonzero signal will suppress the likelihood, allowing to exclude points on the $(m_0, m_{1/2})$ plane almost independently of the exact value of the signal. The likelihood map corresponding to such a case will show a smoothly dropping likelihood function. On the contrary, if the number of observed events is much bigger than the predicted background yield, then the relation $o_i \approx s_i + (b_i \pm \delta b_i)$ can hold only for the nonzero signal (contributions from the background with more than 3σ error will be suppressed by the Gaussian factor). For such points, the Poisson likelihood (9) will be enhanced by the nonzero signal, which will result in the presence of spurious peaks in the likelihood map. In order to reduce the statistical significance of event excess over the background, instead of the Gaussian distribution a correct way to proceed is to model the background uncertainties with a distribution that assigns

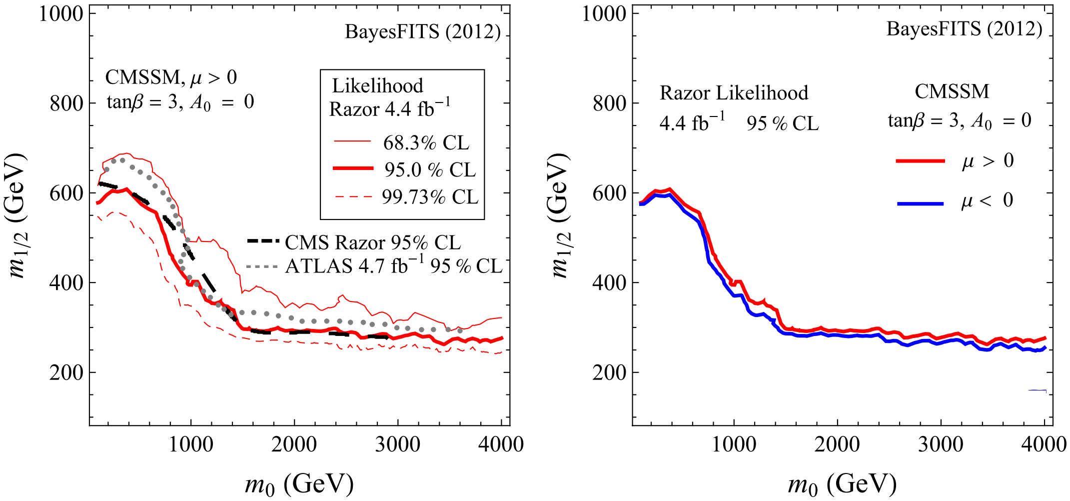

(a) $\mu > 0$. (b) $\mu < 0$.

FIG. 1 (color online). (a) Our approximation of the CMS razor 4.4/fb likelihood map as described in the text. $\tan\beta$ and A_0 are fixed to the values in the legend. The thick solid line shows the 95.0% CL (2σ) bound. It approximates the CMS 95% CL exclusion contour, shown by the dashed black line. The thin solid line and the thin dashed line show our calculations of the 68.3% CL (1σ) and 99.73% CL (3σ) exclusion bound, respectively. The dotted gray line shows the ATLAS 95% CL exclusion bound. (b) Our calculation of the CMS razor 95% CL exclusion line for $\mu > 0$ (red) and $\mu < 0$ (blue).

higher probabilities to the distribution right tail, for example, with a log-normal distribution

$$F(\bar{b}_i|b_i, \delta b_i) = \frac{1}{\bar{b}_i \cdot \delta b_i \cdot \sqrt{2\pi}} \exp\left[-\frac{(\ln\bar{b}_i - b_i)^2}{2 \cdot \delta b_i^2}\right]. \quad (11)$$

With such a distribution one can accommodate larger deviations from the background's central value, which allow to maximalize the total likelihood with a smaller number of signal events and, at the same time, do not suppress the likelihood through convolution. Such an approach allows us to eliminate the spurious peaks in the likelihood map. Note that the presence of the peaks would affect the contribution from the razor limit to the total χ^2, and consequently to $\chi^2_{\rm min}$ and the location of the best-fit point, even at large m_0 and $m_{1/2}$, far above the region excluded by the razor limit (in the large mass region this contribution amounts to approximately three units of χ^2). Such a situation would be clearly unphysical.

On the other hand, note that the procedure that we have adopted here is not unique, even though it correctly reproduces the CMS limit. We will discuss the impact of some other approaches to modeling the razor exclusion limits in Sec. IVA.

The final total likelihood is obtained as a product of likelihoods for each separate bin

$$\mathcal{L}_{\rm razor} = \prod_{i=1}^{38} \mathcal{L}_i. \quad (12)$$

We obtain the 95% CL exclusion limits using the $\Delta\chi^2$ statistics test and validate our result against the official CMS plot [2]. We present in Fig. 1(a) the 68.3% (1σ), 95.0% (2σ) and 99.73% CL (3σ) limits obtained from our likelihood. For comparison we also show the official CMS exclusion limit. We find a very good agreement, provided we rescale our signal by a factor 1.8, which is a reasonable assumption given that PYTHIA calculates the pp cross section at only the leading order,[2] and PGS4 might present some deficit in the efficiency reconstruction.

The approximate efficiency maps derived above allow us to evaluate a likelihood function, so that we can find the regions of the SUSY model's parameter space that are in best agreement with the CMS razor limit. Marked in the figure is also the 95% CL limit from ATLAS, which at low m_0 is actually a bit stronger. We note here that the ATLAS limit was expected to be lower than the razor one in the $(m_0, m_{1/2})$ plane. The actual limit being somewhat higher than expected is a result of downwards fluctuation in the number of background events. Given the fact that the two limits are actually comparable within the experimental resolution around the region where they are located, we will henceforth only show the CMS limit in our figures.

We also verify the influence of selecting the negative sign of μ on our likelihood distribution. While the independence of the exclusion limit of $\tan\beta$ and A_0 in the analysis with all-hadronic final states is a well-known fact, it was never investigated before in the case of $\mu < 0$. The results of such a scan are presented in Fig. 1(b), where we show our

---

[2] The cross section, and consequently the number of expected supersymmetric events, changes by over ten orders of magnitude over the $(m_0, m_{1/2})$ plane. The resulting likelihood function is, therefore, not sensitive to next-to-leading order corrections to the cross section. Even if $\sigma_{\rm NLO} \sim \sigma_{\rm LO}$, the corrections would only slightly shift the isocontours of cross section and likelihood on the $(m_0, m_{1/2})$ plane.

TABLE II. Priors for the parameters of the CMSSM and for the SM nuisance parameters used in our scans. Masses and A_0 are in GeV.

CMSSM parameter	Description	Prior range	Prior distribution
m_0	Universal scalar mass	100, 4000	Log
$m_{1/2}$	Universal gaugino mass	100, 2000	Log
A_0	Universal trilinear coupling	−7000, 7000	Linear
$\tan\beta$	Ratio of Higgs vevs	3, 62	Linear
sgn μ	Sign of Higgs parameter	+1 or −1	Fixed[a]
Nuisance	**Description**	**Central value ± std. dev.**	**Prior distribution**
M_t	Top quark pole mass	172.9 ± 1.1	Gaussian
$m_b(m_b)^{\overline{MS}}_{\rm Sm}$	Bottom quark mass	4.19 ± 0.12	Gaussian
$\alpha_s(M_z)^{\overline{MS}}$	Strong coupling	0.1184 ± 0.0007	Gaussian
$1/\alpha_{\rm em}(M_z)^{\overline{MS}}$	Reciprocal of electromagnetic coupling	127.916 ± 0.015	Gaussian

[a] The sign of parameter μ is fixed for a given scan.

derived razor 95% CL bound. It appears clear that the position of the line in the $(m_0, m_{1/2})$ plane is almost insensitive to the sign of the parameter μ.

C. The Higgs likelihood

In this paper we investigate the impact of the Higgs discovery at the LHC on the CMSSM. In the CMSSM, so long as $m_A \gg m_Z$, the lightest Higgs boson is to a very good accuracy SM-like, i.e., its couplings to ZZ and WW are almost the same as those of the SM Higgs (the so-called decoupling regime) [42]. This has been a conclusion of many previous studies, and has been also carefully checked in Ref. [43] with experimental constraints available at that time (among which the constraints on m_0 and $m_{1/2}$ were clearly weaker than those available now). We will show in Sec. III A that this assumption is justified *a posteriori*, given the present constraints. While the results from the LHC on the Higgs boson do indicate that the discovered boson is indeed SM-like, here we will assume that it is the lightest Higgs boson of the CMSSM that has actually been discovered. Note that in our analysis we will be using information about the Higgs mass but will not be applying constraints on its couplings, in particular on the one to $\gamma\gamma$.

In setting up the Higgs likelihood function one has to take into account an appreciable theoretical error on the light Higgs mass calculation in the MSSM which comes primarily from neglecting higher-order loop corrections, renormalization scheme differences, etc., which is estimated to be around 2–3 GeV [44]. One therefore has to distinguish between the *true* value of the Higgs mass $\hat{m}_h$ which would result from an exact calculation (and which we identify with the physical mass), and the value of the Higgs mass, denoted here by m_h, calculated within a given approximation encoded in one or another spectrum calculator.[3]

The Higgs mass can initially be measured with only a limited precision. We assume that the mass of a SM-like Higgs is measured at $\hat{m}_h = 125$ GeV with a Gaussian experimental uncertainty of $\sigma = 2$ GeV,

$$p(d|\hat{m}_h) = \exp[-(125\ \text{GeV} - \hat{m}_h)^2/2\sigma^2]. \tag{13}$$

Since we have only an imperfect Higgs mass calculation, we assume that the Higgs masses calculated with SOFTSUSY are Gaussian-distributed around the *true* Higgs masses, that is

$$p(\hat{m}_h|m_h) = \exp[-(\hat{m}_h - m_h)^2/2\tau^2], \tag{14}$$

with a theoretical error of $\tau = 2$ GeV.[4] Our likelihood is defined as a convolution of the two functions [34],

$$\mathcal{L}(m_h) = \int p(d|\hat{m}_h) \times p(\hat{m}_h|m_h)\mathrm{d}\hat{m}_h. \tag{15}$$

We choose to add the experimental and theoretical errors in quadrature, finally obtaining

$$\mathcal{L}_{m_h \simeq 125\ \text{GeV}}(m_h) = \exp[-(125\ \text{GeV} - m_h)^2/2(\tau^2 + \sigma^2)]. \tag{16}$$

III. RESULTS

In this section we will present our numerical results. We scanned the parameter space of the CMSSM over the ranges given in Table II. Note that, compared to Ref. [25], we doubled the ranges of m_0 and $m_{1/2}$, which are now the same as in Ref. [26], and we enlarged the range of A_0 from (− 2 TeV, 2 TeV) to (− 7 TeV, 7 TeV) in order to approach $m_h \sim 125$ GeV. As before, we applied a log prior to the mass parameters m_0 and $m_{1/2}$, and a linear one to A_0 and $\tan\beta$. We performed our scans for $\mu > 0$ and

---

[3] In our numerical scans we use SOFTSUSY version 3.2.4 [45] but one should be aware that all available Higgs mass codes presently have similar (or larger) theoretical errors.

[4] Alternatively we could take a linear, rather than Gaussian distribution, which would be much more conservative.

TABLE III. The experimental measurements that we apply to constrain the CMSSM's parameters. Masses are in GeV.

Measurement	Mean or range	Exp. error	Th. error	Likelihood distribution	Ref.
CMS razor 4.4/fb analysis	See text	See text	0	Poisson	[2]
SM-like Higgs mass m_h	125	2	2	Gaussian	[8,9,44]
$\Omega_\chi h^2$	0.1120	0.0056	10%	Gaussian	[46]
$\sin^2\theta_{\rm eff}$	0.23116	0.00013	0.00015	Gaussian	[47]
m_w	80.399	0.023	0.015	Gaussian	[47]
$\delta(g-2)_\mu^{\rm susy} \times 10^{10}$	28.7	8.0	1.0	Gaussian	[47,48]
$\mathrm{BR}(\bar{\mathrm{B}} \to \mathrm{X}_s \gamma) \times 10^4$	3.60	0.23	0.21	Gaussian	[47]
$\mathrm{BR}(\mathrm{B}_u \to \tau\nu) \times 10^4$	1.66	0.66	0.38	Gaussian	[49]
ΔM_{B_s}	17.77	0.12	2.40	Gaussian	[47]
$\mathrm{BR}(\mathrm{B}_s \to \mu^+\mu^-)$	$<4.5 \times 10^{-9}$	0	14%	Upper limit—Error Fn	[23]

$\mu < 0$ separately, for each case with and without the $(g-2)_\mu$ constraint.

In the current analysis we have improved our treatment of the SM nuisance parameters. In our previous analyses, we sampled the nuisance parameters from finite linear intervals (linear priors), and included Gaussian likelihood functions that described their experimental measurements. In this analysis, we sample the nuisance parameters directly from Gaussian priors that describe their experimental measurements and do not include them into the likelihood function. This improves our algorithm's efficiency and is a more intuitive method.

The experimental constraints applied in our scans are listed in Table III. In comparison with our previous papers Refs. [25,26], the new upper limit on $\mathrm{BR}(\mathrm{B}_s \to \mu^+\mu^-)$ is used, which is evidently more constraining than the old one. Note also that LEP and Tevatron limits on the Higgs sector and superpartner masses are not listed in Table III because the subsequent LHC limits were generally stronger, and in any case in this paper we consider only the case of the Higgs signal. The razor and Higgs limits are included as described in Sec. II.

In Ref. [26] we showed that the effect of the current limits from FermiLAT and XENON100 strongly depends on a proper treatment of astrophysical uncertainties. If the uncertainties are treated in a conservative way, both direct and indirect limits from DM searches are not more constraining than the accelerator ones, hence we ignore them in the present analysis.

We have developed a new numerical code, BayesFITS, similar in spirit to the MasterCode [50] and Fittino [51] frameworks (which perform frequentist analyses), and to SuperBayeS [52] and PYSUSY[5] (which perform Bayesian analyses). BayesFITS engages several external, publicly available packages: for sampling it uses MULTINEST [53] with 4000 live points, evidence tolerance factor set to 0.5, and sampling efficiency equal to 0.8. The mass spectrum is computed with SOFTSUSY and written in the form of SUSY Les Houches Accord files, which are then taken as input files to compute various observables. We use SUPERISO RELIC V3.2 [54] to calculate $\mathrm{BR}(\bar{\mathrm{B}} \to \mathrm{X}_s\gamma)$, $\mathrm{BR}(\mathrm{B}_s \to \mu^+\mu^-)$, $\mathrm{BR}(\mathrm{B}_u \to \tau\nu)$, and $\delta(g-2)_\mu^{\rm SUSY}$, and FeynHiggs 2.8.6 [55] to calculate the electroweak variables m_W, $\sin^2\theta_{\rm eff}$, and ΔM_{B_s}. The DM observables, such as the relic density and direct detection cross sections, are calculated with MicrOMEGAS 2.4.5 [56].

Below we will present the results of our scans as one-dimensional (1D) or two-dimensional (2D) marginalized posterior pdf maps of parameters and observables. In evaluating the posterior pdf's, we marginalize over the given SUSY model's other parameters and the SM's nuisance parameters, as mentioned above and described in detail in Refs. [25,26].

A. The CMSSM with $(g-2)_\mu$

In Figs. 2(a) and 2(b) we show the marginalized posterior pdf in the $(m_0, m_{1/2})$ plane and in the $(A_0, \tan\beta)$ plane, respectively. In these and the following plots we show the Bayesian 68.3% (1σ) credible regions in dark blue, encircled by solid contours, and the 95% (2σ) credible regions in light blue, encircled by dashed contours.

The posterior presented in Fig. 2(a) features a bimodal behavior, with two well-defined 1σ credible regions. One mode, smaller in size, which is located at small m_0, is the $\tilde{\tau}$-coannihilation region, whereas a much more extended mode lies in the A-funnel region. Although the bimodal behavior is superficially similar to what was already observed in Ref. [25], there are substantial differences. Most notably, the high probability mode which, in that paper and in Ref. [26], was spread over the focus point (FP)/hyperbolic branch (HB) region at large m_0 and $m_{1/2} \ll m_0$, has now moved up to the A-funnel region.

The reason for the different behavior of the posterior with respect to Ref. [25] is twofold. On the one hand, we have found that the highest density of points with the right Higgs mass can be found at $m_{1/2} \gtrsim 1$ TeV, which moves the posterior credible regions up in the plane. On the other hand, some points with a large m_h can also be

---

[5] Written by Andrew Fowlie, public release forthcoming, see http://www.hepforge.org/projects.

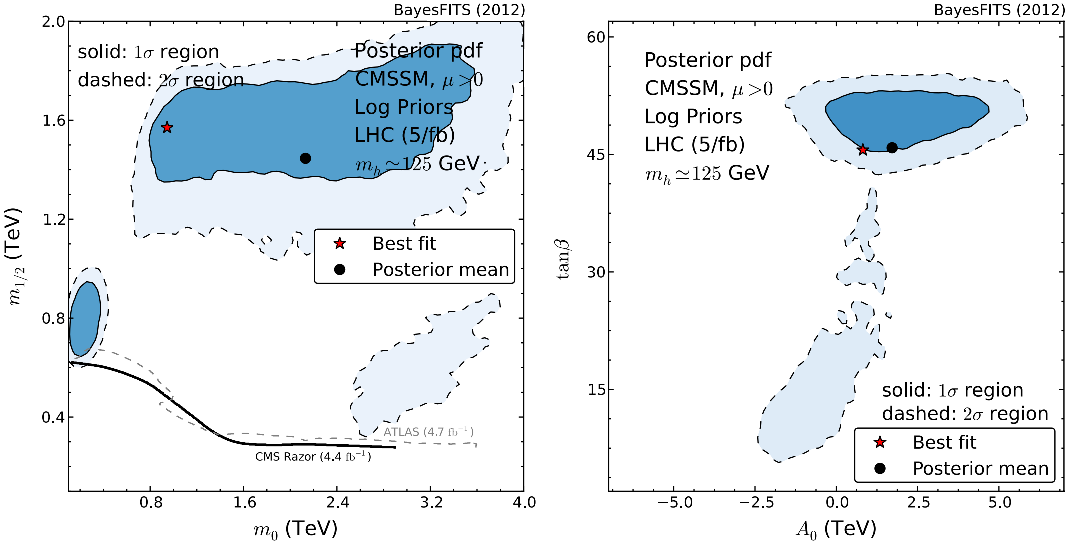

(a) (b)

FIG. 2 (color online). Marginalized posterior pdf in (a) the (m_0, $m_{1/2}$) plane and (b) the (A_0, $\tan\beta$) plane of the CMSSM, constrained by the experiments listed in Table III. The solid black line shows the CMS razor 95% CL exclusion bound.

found in the FP/HB region but the scan tends to ignore them in favor of points in the A-funnel region over which the b-physics constraints are better satisfied. The new upper bound on BR($B_s \to \mu^+\mu^-$) from LHCb also yields a substantial contribution. The approximately rectangular region bounded by $m_0 \sim 500$–2000 GeV and $m_{1/2} \sim 400$–1000 GeV is now cut out at the 95% CL. Notice that in our previous papers [25,26] the same part of parameter space was included in the 95% credible region.

The new 4.4/fb razor exclusion bound reduces the size of the 1σ credible region of $\tilde{\tau}$-coannihilation at small m_0, with respect to what was observed in our previous analyses [25,26], where we used the 1.1/fb α_T likelihood. The razor constraint also excludes more of the FP/HB region. We point out here that the improved exclusion bound on $m_{1/2}$ in the $\tilde{\tau}$-coannihilation region is mostly due to the increased luminosity, while in the FP/HB region to switching from the α_T to the razor search. The razor bound with 0.8/fb luminosity [3] was better than the α_T bound in the FP/HB region, but worse in the $\tilde{\tau}$-coannihilation region, where the improvement due to luminosity is more dramatic. As a matter of fact, in the $\tilde{\tau}$-coannihilation the dominant cross section is $pp \to \tilde{q}\,\tilde{q}$, while in the FP/HB region it is $pp \to \tilde{g}\,\tilde{g}$. M_R is in all effect an estimate of the difference $m_{\tilde{g}(\tilde{q})} - m_\chi$. Since in the CMSSM the gluino and LSP masses are correlated, the sensitivity in the FP/HP region does not increase with luminosity as fast as in the region at small m_0. Finally, we note that, in this case, the best-fit point is located on the left-hand side of the A-funnel region. We postpone further discussion of χ^2_{min} and the stability of the location of the best-fit point until Sec. IV.

A similar bimodal behavior of the marginalized posterior can be observed in Fig. 2(b). The large 1σ credible region at $\tan\beta \sim 45$–55 corresponds to the large 1σ region in the A-funnel of the (m_0, $m_{1/2}$) plane. Conversely, the 2σ region at $A_0 \sim 0$ and $\tan\beta \lesssim 30$ can be mapped back to the $\tilde{\tau}$-coannihilation region of the (m_0, $m_{1/2}$) plane. In Refs. [25,26] we could observe a wide 1σ credible region at intermediate $\tan\beta$, whose statistical relevance has now decreased. It corresponds to the FP/HB region of the (m_0, $m_{1/2}$) plane, now disfavored by the new LHC constraints on the Higgs mass.

Since BR($B_s \to \mu^+\mu^-$) is proportional to $\tan^6\beta/m_A^4$, one could have naively expected to see small values of $\tan\beta$ favored by the new upper bound from LHCb. As we can see in Fig. 2(b), this is actually not the case. This is because some other constraints favor large $\tan\beta$. One is $\delta(g-2)_\mu^{\mathrm{SUSY}}$, even though at the end it is poorly satisfied. The other is a combination of the relic density favoring also larger m_A with the light Higgs mass close to 125 GeV, both of which can be more easily achieved at large $m_{1/2}$. The end result is that m_A is now required to be larger than in the past, which is consistent with the observed prevalence of the A-funnel region over the FP/HB region.

The 1D relative marginalized posteriors for the masses of selected superpartners are shown in the four panels of Fig. 3. In Fig. 3(a) one can see the posterior for the lightest stop mass; in Fig. 3(b) the one for the heaviest squark, $\tilde{u}_L$; Figs. 3(c) and 3(d) show the gluino and lightest neutralino, respectively. As we mentioned in the previous section, the razor method will translate a lower bound on M_R and R^2 into a lower bound on squark and gluino masses. At small m_0, where the cross section for $pp \to \tilde{q}\,\tilde{q}$ is dominant, this translates into $m_{\tilde{t}_1} \gtrsim 800$ GeV and $m_{\tilde{u}_L} \gtrsim 1200$ GeV; at large m_0, where $pp \to \tilde{g}\,\tilde{g}$ dominates, the razor sets the limit $m_{\tilde{g}} \gtrsim 800$ GeV.

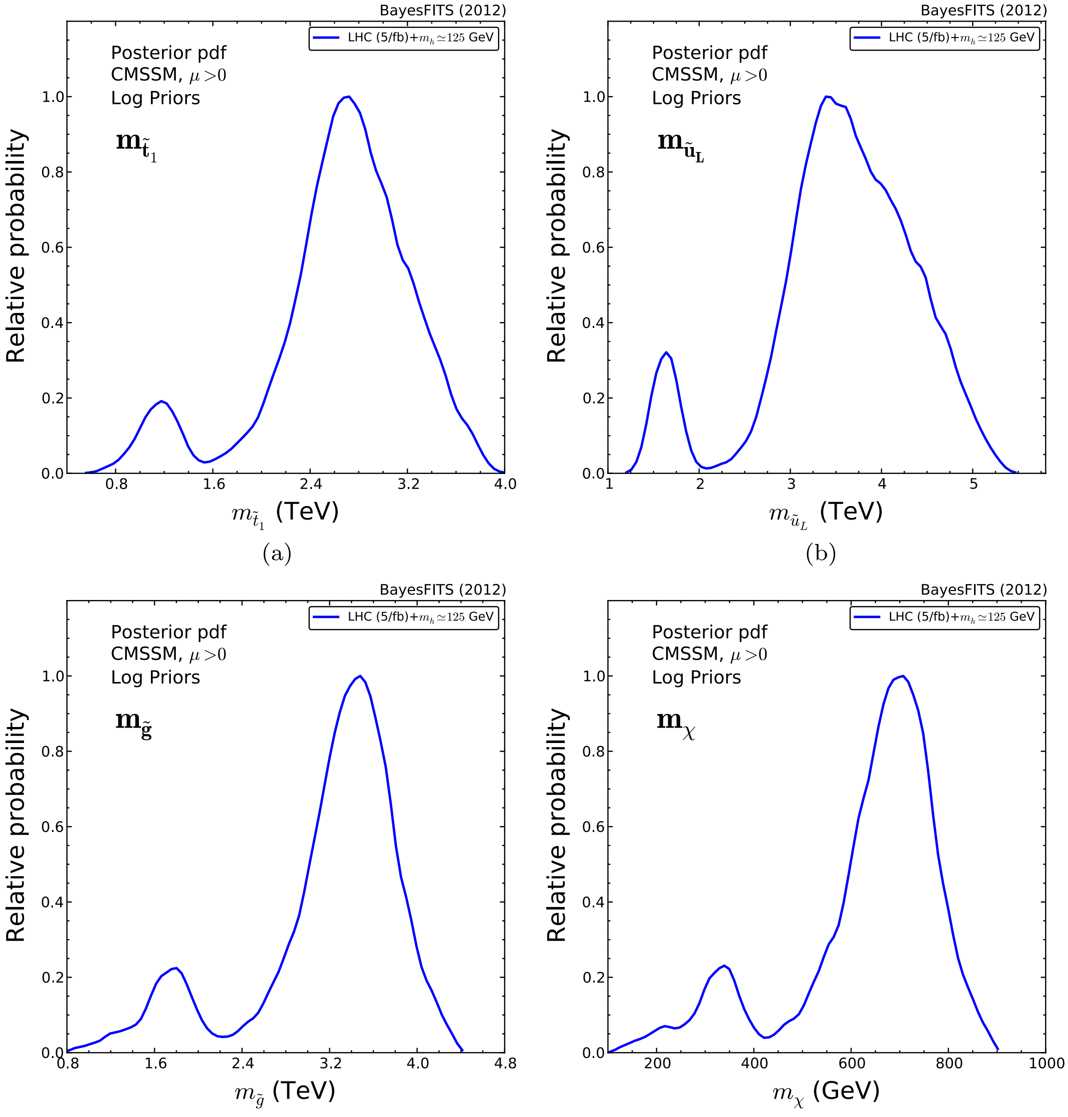

(a) (b)

(c) (d)

FIG. 3 (color online). One-dimensional marginalized posterior pdf for the mass of (a) the lightest stop, (b) the $\tilde{u}_L$ squark, (c) the gluino, and (d) the lightest neutralino in the CMSSM constrained by the experiments listed in Table III.

The highest peaks, indicating the values most favored by the present constraints, are located at $m_{\tilde{t}_1} \sim 2.5$ TeV, $m_{\tilde{u}_L} \sim 3.2$ TeV, $m_{\tilde{g}} \sim 3.2$ TeV, and $m_\chi \sim 700$ GeV. The relative probability of the peaks obtained in the A-funnel region is higher than the probability of the peaks obtained in the $\tilde{\tau}$-coannihilation region. We show in Fig. 4 the one-dimensional posteriors for all particles in the supersymmetric spectrum.

Figure 5(a) shows the two-dimensional posterior in the (A_0, m_h) plane. It presents an interesting behavior, not often pointed out in the literature. Given the experimental and theoretical uncertainties on the Higgs mass determination, the Bayesian fit to all constraints favors positive values of A_0, although we confirm the known fact that $m_h > 123$ GeV can be more easily obtained in the CMSSM only for negative values of A_0.

Figure 5(b) shows the posterior in the $(m_A, \tan\beta)$ plane. As mentioned above, the combined effect of the new Higgs constraints and $\mathrm{BR}(B_s \to \mu^+\mu^-)$ now favors larger values of both parameters. Notice that the $(m_A, \tan\beta)$ range encompassed by the high posterior probability contours safely place the model in the decoupling regime (Sec. II C) and thus justify our assumption of a SM-like Higgs.

In Fig. 6(a) we show the 2D posterior in the $\delta(g-2)_\mu^{\mathrm{SUSY}}$ versus $\mathrm{BR}(\bar{B} \to X_s\gamma)$ plane for $\mu > 0$. The $(g-2)_\mu$ constraint is applied. The red horizontal line (dot-dashed) shows the experimental value of $\mathrm{BR}(\bar{B} \to X_s\gamma)$, and the pink shaded region highlights the experimental uncertainties at 1σ. The blue horizontal line (dotted) shows the SM value, as calculated by SuperISO. One can see that the 68% and 95% Bayesian credible regions are consistent with the experimental value of $\mathrm{BR}(\bar{B} \to X_s\gamma)$ at the 2σ level,

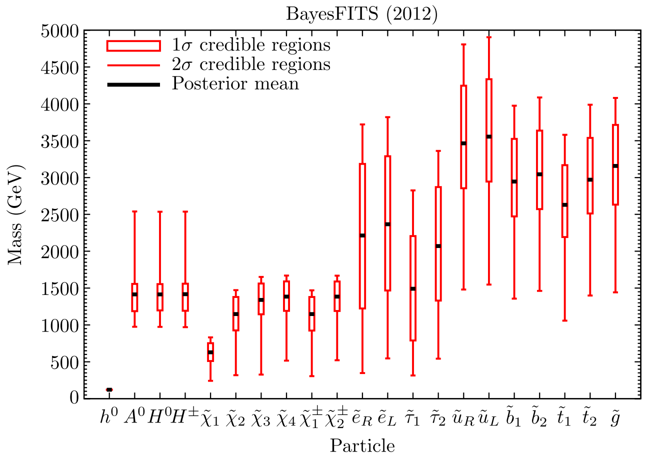

FIG. 4 (color online). One-dimensional marginalized posterior pdf for the supersymmetric spectrum constrained by the experiments listed in Table III.

while $\delta(g-2)_\mu^{\rm SUSY}$ shows a poor fit, as was noticed in many previous global scans of the CMSSM; see, e.g., Refs. [15,26,27,34]. In particular, for $\mu > 0$, a slightly better fit to $\delta(g-2)_\mu^{\rm SUSY}$ is obtained in the $\tilde\tau$-coannihilation region, which implies values of $\mathrm{BR}(\bar{\mathrm{B}} \to \mathrm{X_s}\gamma)$ closer to the SM value, which lies $\sim 1.5\sigma$ away from the measured one [34]. On the other hand, the best-fit point lies in the A-funnel region, where it is harder to satisfy $(g-2)_\mu$ but easier to satisfy $\mathrm{BR}(\bar{\mathrm{B}} \to \mathrm{X_s}\gamma)$

Figure 6(b) shows that a similar tension exists between the $\mathrm{BR}(\mathrm{B_s} \to \mu^+\mu^-)$ and $(g-2)_\mu$ constraints. The red line (dot-dashed) shows the new LHCb 95% CL upper bound, while the blue line (dotted) shows the SM value for $\mathrm{BR}(\mathrm{B_s} \to \mu^+\mu^-)$ that we use in our calculations. In an attempt to better fit the $(g-2)_\mu$ constraint, a narrow 95% credible region shows up along the SM values of $\mathrm{BR}(\mathrm{B_s} \to \mu^+\mu^-)$, which lie in the $\tilde\tau$-coannihilation region where $\tan\beta$ is smaller. However, the best-fit point is situated in the A-funnel region, where the $(g-2)_\mu$ constraint is overcome by the one due to $\mathrm{BR}(\mathrm{B_s} \to \mu^+\mu^-)$, which is now free to assume a broader range of values.

The probability distribution of the lightest Higgs mass is shown in Fig. 7(a). The present constraints highly favor Higgs masses centered around $m_h \sim 122$ GeV. Points having $m_h > 124$ GeV are difficult to achieve in the CMSSM with the prior ranges we consider ($m_0 \lesssim 4$ TeV, $m_{1/2} \lesssim 2$ TeV), as is well known. They are, nonetheless, present in our chain in appreciable number but they are disfavored by the global constraints. This point is made clear in Fig. 7(b), where we show a scatter plot of the total χ^2 versus the Higgs mass. Points giving Higgs masses as large as 125 GeV are generated, but their global fit to all constraints is generally poor.

The reason for so strongly disfavoring larger values of m_h is the tension between the Higgs mass above 124 GeV and the correct value of the relic density. This tension manifests itself both in the A-funnel and in the FP/HB region, though its origin in each of those regions is different. In the A-funnel the main mechanism that allows to obtain the correct value of the relic density is the resonance annihilation of neutralinos through the pseudoscalar A boson. To allow such a process, an approximate relation $m_A \sim 2m_\chi$ should hold. However, for cases where $m_h > 124$ GeV the mass of the pseudoscalar m_A exceeds significantly the doubled mass of the neutralino, and annihilation at the resonance cannot take place.

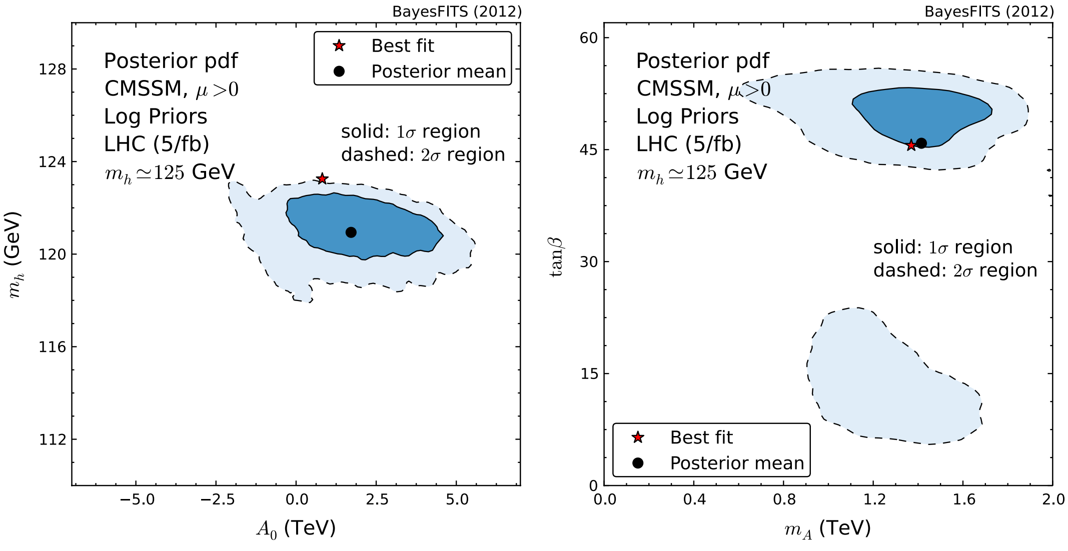

(a) (b)

FIG. 5 (color online). Marginalized posterior pdf in the (A_0, m_h) plane, in the CMSSM constrained by the experiments listed in Table III. (b) Marginalized posterior pdf in the $(m_A, \tan\beta)$ plane for the same constraints.

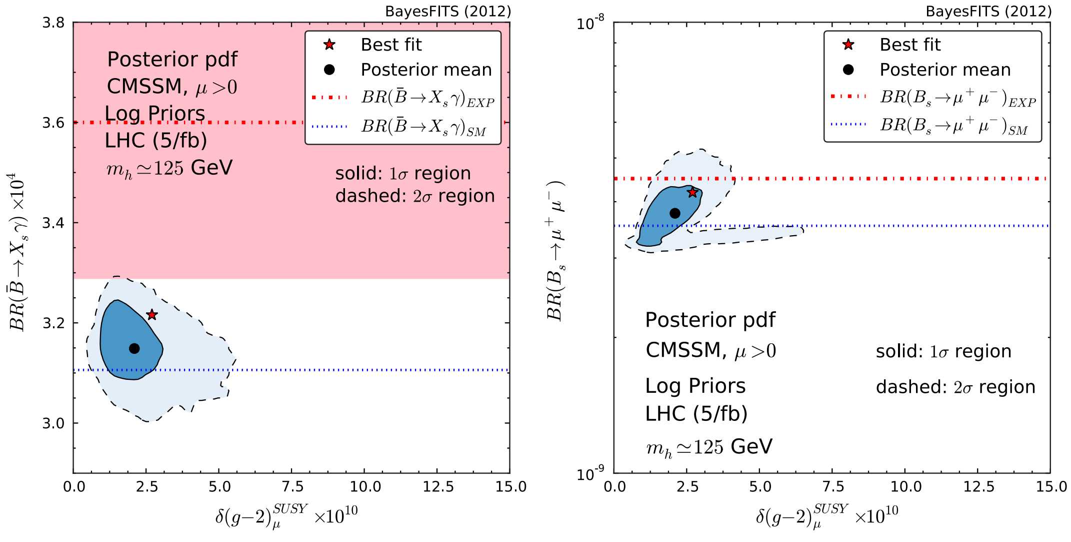

(a) (b)

FIG. 6 (color online). (a) Marginalized posterior pdf of the experimental observables $\delta(g-2)_\mu^{\mathrm{susy}}$ versus $\mathrm{BR}(\bar{\mathrm{B}}\to\mathrm{X_s}\gamma)$ in the CMSSM constrained by the experiments listed in Table III. (b) Marginalized posterior pdf of the experimental observables $\delta(g-2)_\mu^{\mathrm{susy}}$ versus $\mathrm{BR}(\bar{\mathrm{B}}\to\mathrm{X_s}\gamma)$ under the same constraints.

In the FP/HB region the correct relic density is achieved in another way. Because of the relatively small values of $|\mu|$ the lightest neutralino becomes more Higgsino-like, and the annihilation cross section is enhanced. However, as we have already stated, in the CMSSM the lightest Higgs boson with mass larger than 124 GeV can be much more easily obtained for large ($\lesssim -1$ TeV) negative values of A_0 at the GUT scale. After running down to the electroweak scale, negative values for A_0 yield even larger negative A_t, which is one of the conditions to obtain large Higgs boson masses, as it will appear clear below. On the other hand, taking into account the minimalization condition for the scalar potential, large negative A_0 do not allow the parameter μ to be small enough to enhance the Higgsino-like component of the neutralino. That creates the tension between the relic density and the Higgs mass above 124 GeV.

In Fig. 8(a) we show a scatter plot representing the distribution of the lightest Higgs mass over the $(m_0, m_{1/2})$, plane. One can see that Higgs masses compatible with 125 GeV at 1σ can be obtained in large numbers across the whole plane. Particularly, the mass distribution presented in Fig. 8(a) has one interesting aspect. The one-loop contribution to the Higgs mass in the decoupling limit ($m_A \gg m_z$) for moderate-to-large $\tan\beta$ is given by [57]

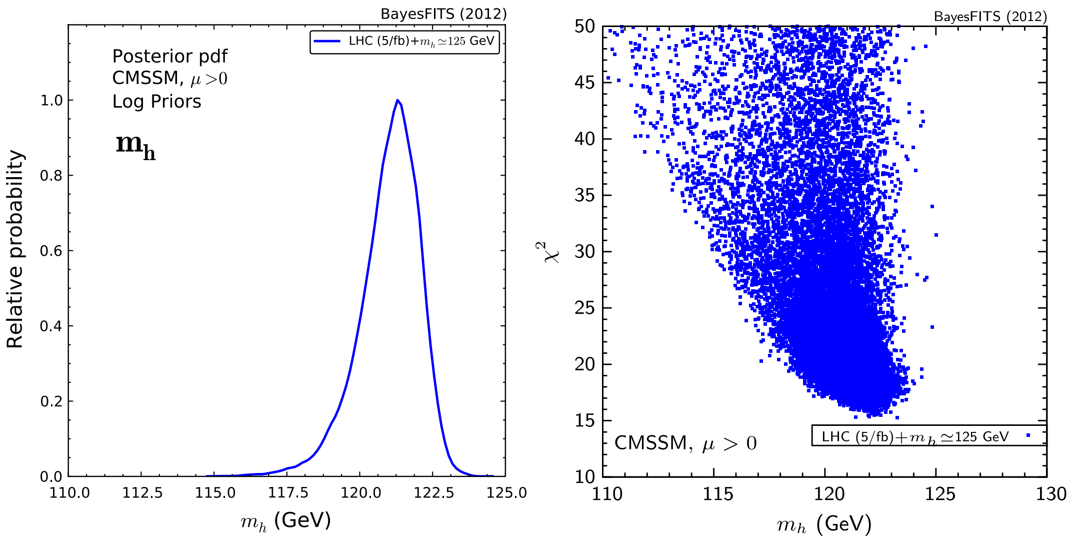

(a) (b)

FIG. 7 (color online). (a) Marginalized 1D posterior pdf of m_h in the CMSSM constrained by the experiments listed in Table III. (b) Scatter plot showing the distribution of the total χ^2 of the points in our chain versus the Higgs mass.

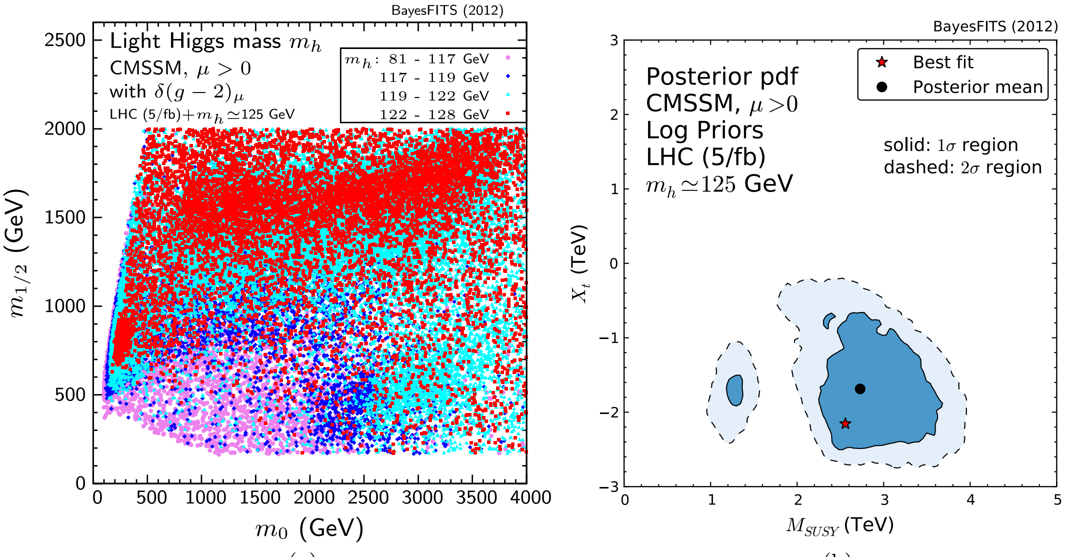

(a) (b)

FIG. 8 (color online). (a) Scatter plot showing the value of m_h in the $(m_0, m_{1/2})$ plane of the CMSSM. (b) Marginalized posterior pdf in the parameters X_t versus M_{SUSY}, relevant for the loop corrections to the Higgs mass.

$$\Delta m_h^2 \propto \ln\frac{M_{\mathrm{SUSY}}^2}{m_t^2} + \frac{X_t^2}{M_{\mathrm{SUSY}}^2}\left(1 - \frac{X_t^2}{12M_{\mathrm{SUSY}}^2}\right), \tag{17}$$

where m_t is the top quark mass, M_{SUSY} is the geometrical average of the physical stop masses, and $X_t = A_t - \mu \cot\beta$. While the presence of a relatively heavy Higgs is not a surprise in the A-funnel region, where the one-loop contribution to m_h is driven up by a large SUSY scale, it is more striking in the $\tilde{\tau}$-coannihilation region. As anticipated above, to ensure such a heavy Higgs mass in the region of low m_0 and $m_{1/2}$, the contribution from the X_t factor in Eq. (17) should be significant. ($X_t \sim A_t$ almost throughout the whole parameter space.) In fact, it turns out that the $\tilde{\tau}$-coannihilation region is the only region of parameter space where the factor $|X_t|/M_{\mathrm{SUSY}}$ reaches values close to $\sim$2.5, the maximal contribution from the stop-mixing.

The interplay between M_{SUSY} and X_t just described is often claimed in the literature to be an indication of fine-tuning [58], thus making the CMSSM a less natural model than, for instance, the Next-to-Minimal Supersymmetric Standard Model [17]. We plot in Fig. 8(b) the two-dimensional marginalized posterior in the (M_{SUSY}, X_t) plane. One can see two separate high-probability regions. The one on the right corresponds to the A-funnel region, where the best-fit point lies, while the one on the left, smaller in size, to the $\tilde{\tau}$-coannihilation region. We gather that, even if the model might be intrinsically fine-tuned, given the present status of experimental and theoretical uncertainties, our global set of constraints favors 2σ credible regions that span an area of $\sim$10 TeV^2, thus allowing a broad range of values for these parameters. Moreover, it appears clear that the present set of constraints highly favors negative values of X_t.

B. Impact of $(g-2)_\mu$ and the case $\mu < 0$

Since the poor global fit is mainly a result of including the $(g-2)_\mu$ constraint in the likelihood, and the SM prediction is to this day still marred by substantial theoretical uncertainties, we have also performed scans without the $(g-2)_\mu$ constraint. In this case there is no reason anymore to assume $\mathrm{sgn}\,\mu = +1$, as the main reason for such choice was to improve the fit to this particular observable. For this reason we will not show the case with $(g-2)_\mu$ and $\mu < 0$ because the global fit worsens, although actually not so much. We will summarize the goodness of all the fits in Table IV.

Before we move to the case with no $(g-2)_\mu$, a few remarks on the effect of reversing sgn μ while maintaining the $(g-2)_\mu$ constraint are in order. Even with $(g-2)_\mu$ taken into account, we checked that the main effect of taking $\mu < 0$ would impact on the value and location of the best-fit point, rather than the posterior distribution. The probability distributions obtained in this case are very similar to the ones depicted in Fig. 2, but the best-fit point is now pushed up to larger m_0 and $m_{1/2}$. Clearly, when μ is negative, the $(g-2)_\mu$ constraint tends to favor large mass scales, since it tends to minimize the (now negative) contribution. On the other hand, the change in the sign of μ allows almost all points in the scan to satisfy $B_s \to \mu^+\mu^-$, and this provides a significant difference from the cases with positive μ, where a relatively wide region of parameter space at small m_0 and $m_{1/2}$ was disfavored under the new LHCb limit. These two contrasting effects can be thought as balancing out, thus producing a similar posterior distribution.

Let us now analyze the effects of lifting the $(g-2)_\mu$ constraint. The case $\mu > 0$ is shown in Fig. 9(a), where we plot the two-dimensional posterior in the $(m_0, m_{1/2})$

TABLE IV. Breakdown of all contributions to the χ^2 of the best-fit points of our four different CMSSM likelihood scans.

	Contribution to χ^2_{min}	$\Omega_\chi h^2$	m_h	$\bar{B} \to X_s\gamma$	$B_s \to \mu^+\mu^-$	$\sin^2\theta_{\text{eff}}$	m_w	$\delta(g-2)_\mu^{\text{susy}}$	$(B_\mu \to \tau\nu)$	ΔM_{B_s}	razor	Total
1	with $(g-2)_\mu$, $\mu > 0$	0.10	0.38	1.52	0.70	1.07	0.13	10.40	0.85	0.12	0.14	15.42
2	with $(g-2)_\mu$, $\mu < 0$	0.06	0.70	0.00004	0	0.21	0.14	13.93	0.91	0.46	0.14	16.56
3	w/o $(g-2)_\mu$, $\mu > 0$	0.15	0.74	1.37	0.08	0.05	0.44	...	0.84	0.16	0.14	3.97
4	w/o $(g-2)_\mu$, $\mu < 0$	0.15	0.33	0.12	0	0.31	0.06	...	0.93	0.70	0.14	2.74

plane, and in Fig. 9(c) where the distribution in the $(A_0, \tan\beta)$ plane is shown. The plots do not show much difference from the cases with $(g-2)_\mu$ included. The best-fit point moves towards larger m_0, and one can notice the slightly increased relevance of the FP/HB region. The near independence of the global posterior distribution of the $(g-2)_\mu$ constraint for $\mu > 0$ was to be expected. As one can see in Table IV, the contribution to the total χ^2 of the best-fit point due to this constraint is by far the largest, thus making it the observable most

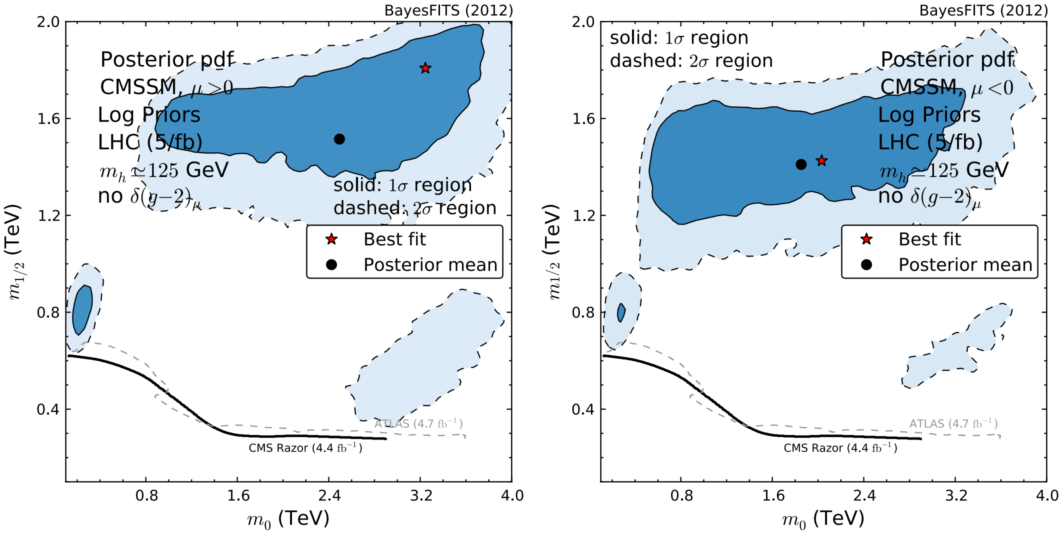

(a) $\mu > 0$ and no $(g-2)_\mu$. (b) $\mu < 0$ and no $(g-2)_\mu$.

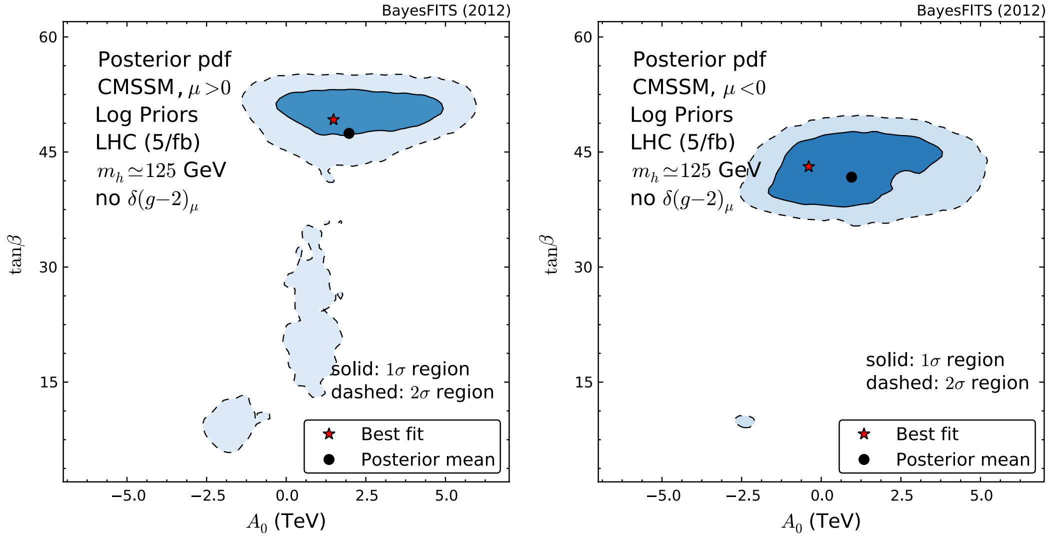

(c) $\mu > 0$ and no $(g-2)_\mu$. (d) $\mu < 0$ and no $(g-2)_\mu$.

FIG. 9 (color online). (a) Marginalized posterior pdf in the $(m_0, m_{1/2})$ plane for the constraints listed in Table III except $(g-2)_\mu$, for $\mu > 0$. (b) Marginalized posterior pdf in the $(m_0, m_{1/2})$ plane for the same constraints as in (a) and $\mu < 0$. (c) Marginalized posterior pdf in the $(A_0, \tan\beta)$ plane for the same constraints as in (a). (d) Marginalized posterior pdf in the $(A_0, \tan\beta)$ plane for the same constraints as in (a) and $\mu < 0$.

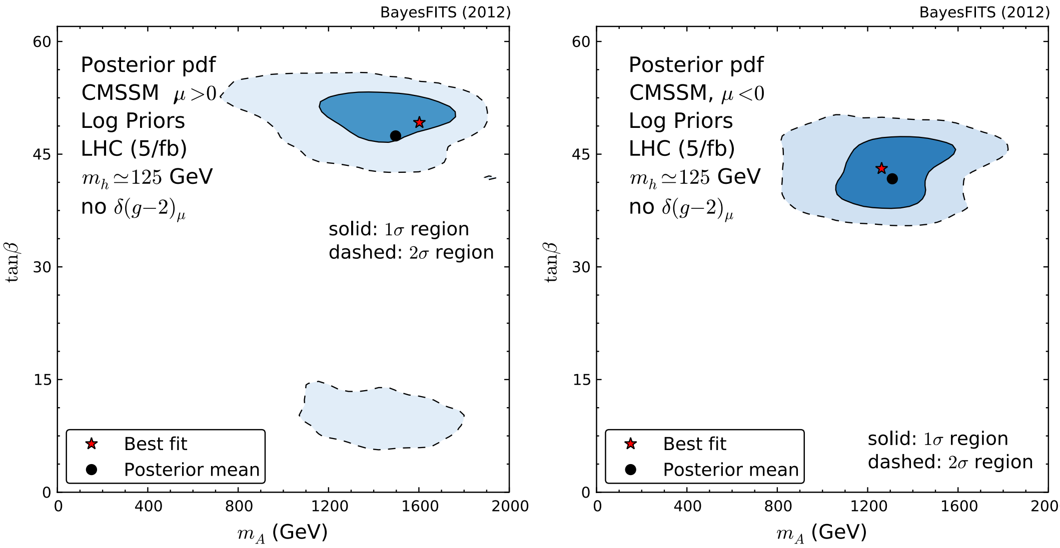

(a) (b)

FIG. 10 (color online). Marginalized posterior pdf in the $(m_A, \tan\beta)$ plane, in the CMSSM constrained by all the experiments listed in Table III except $(g-2)_\mu$. (a) $\mu > 0$, (b) $\mu < 0$.

poorly fit. When all other constraints pull in a different direction, the pdf becomes insensitive to this constraint, in all effects treating it as an outlier.

In fact, when $(g-2)_\mu$ is ignored, the lowest χ^2 for all the four cases we have studied, is obtained with negative μ. We show the marginalized posterior for this case in the $(m_0, m_{1/2})$ plane in Fig. 9(b). One can see that the area of parameter space corresponding to the A-resonance region extends to values of m_0 lower than in the other cases; the $\tilde{\tau}$ and FP/HB regions are instead reduced. As described above, $\mu < 0$ allows to satisfy $\mathrm{BR}(\mathrm{B_s} \to \mu^+\mu^-)$ in broader regions of parameter space. Moreover, it appears that the Higgs mass constraint can be satisfied better in the low m_0 region for $\mu < 0$. When it comes to the marginalized posterior in the $(m_0, m_{1/2})$ plane [shown in Fig. 9(d)] one can see that low values of $\tan\beta$ are nearly excluded, and the 1σ credible region has shifted down, to values around $\tan\beta \sim 40$–45.

In Fig. 10(a) we show the two-dimensional pdf in the $(m_A, \tan\beta)$ plane without the $(g-2)_\mu$ constraint, and taking $\mu > 0$. No visible difference appears with the case which included $(g-2)_\mu$. Significant differences appear instead for $\mu < 0$, as shown in Fig. 10(b). Not only can one notice the down-shifting of the preferred values for

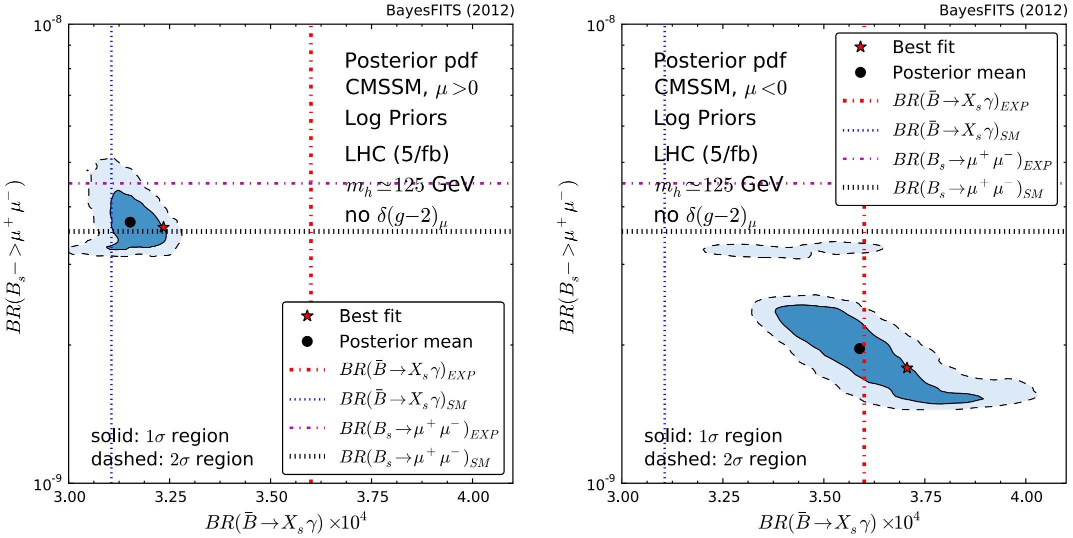

(a) (b)

FIG. 11 (color online). Marginalized posterior pdf of the experimental observables $\mathrm{BR}(\bar{\mathrm{B}} \to \mathrm{X_s}\gamma)$ versus $\mathrm{BR}(\mathrm{B_s} \to \mu^+\mu^-)$ in the CMSSM constrained by all the experiments listed in Table III except $(g-2)_\mu$. (a) $\mu > 0$, (b) $\mu < 0$.

$\tan\beta$ mentioned above, but also lower values of m_A than in the positive μ case are now favored at large $\tan\beta$. The reason lies in the improved fit to the b-physics observables, and in particular to $\mathrm{BR}(B_s \to \mu^+\mu^-)$.

This can be seen in Fig. 11 where we show the two-dimensional posterior for the observables $\mathrm{BR}(\bar{B} \to X_s\gamma)$ versus $\mathrm{BR}(B_s \to \mu^+\mu^-)$ for (a) $\mu > 0$ and (b) $\mu < 0$. The purple horizontal line (dot-dashed) and the red vertical line (dot-dashed) show the respective experimental values, while the horizontal gray line (dotted) and the vertical blue line (dotted) show the respective SM values. One can see that, for $\mu > 0$ the probability distribution does not change significantly when we lift the $(g-2)_\mu$ constraint. It confirms the fact that, given the poorness of the fit to $\delta(g-2)_\mu^{\mathrm{SUSY}}$, the posterior is effectively insensitive to this constraint.

However, again, a significant difference arises for the case with $\mu < 0$, shown in Fig. 11(b). The contribution from the chargino-stop loop to $\mathrm{BR}(\bar{B} \to X_s\gamma)$ changes sign and now contributes positively to alleviate the discrepancy between the experimental and the SM value. As a consequence, the overall fit to the experimental measurement improves, with the exception of the region at small m_0 and $m_{1/2}$ where the value becomes a bit too high. $\mathrm{BR}(B_s \to \mu^+\mu^-)$ gets instead negative contributions that improve the fit over all parameter space, even pushing the preferred value below the SM calculation.

In Fig. 12(a) we show the one-dimensional marginalized posterior on Higgs mass distribution in the case without $(g-2)_\mu$ and $\mu < 0$. In Fig. 12(b) we show a scatter plot of the distribution of Higgs masses over the $(m_0, m_{1/2})$ plane. Basically no difference in the distribution of the Higgs mass is found for $\mu < 0$. Finally, Fig. 13 shows the Bayesian credibility regions for the supersymmetric spectrum when the $(g-2)_\mu$ constraint is lifted for $\mu > 0$ (a) and $\mu < 0$ (b).

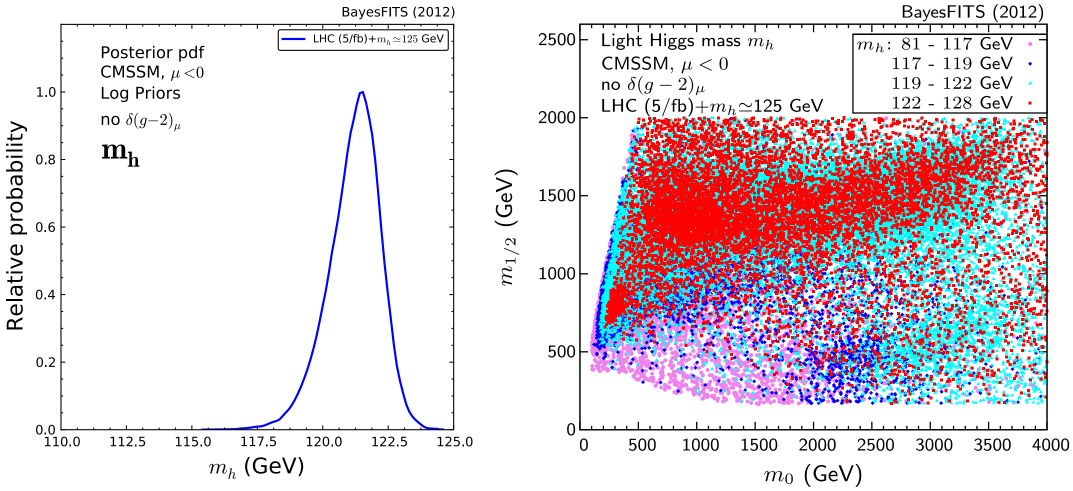

(a) (b)

FIG. 12 (color online). (a) Marginalized 1D posterior pdf of m_h for $\mu < 0$, constrained by the experiments listed in Table III except $(g-2)_\mu$. (b) Scatter plot distribution of the Higgs mass in the $(m_0, m_{1/2})$ plane without the $(g-2)_\mu$ constraint, $\mu < 0$.

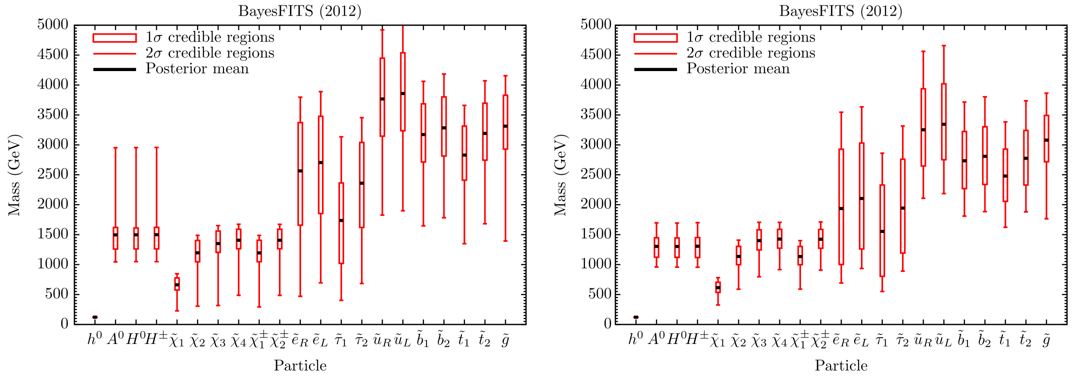

(a) $\mu > 0$ (b) $\mu < 0$

FIG. 13 (color online). 1D marginalized posterior pdf for the supersymmetric spectrum constrained by the experiments listed in Table III except $(g-2)_\mu$. (a) $\mu > 0$. (b) $\mu < 0$.

C. Dark matter direct detection and μ combination

In Fig. 14 we show a combination of the $\mu > 0$ and $\mu < 0$ cases, without the $(g-2)_\mu$ constraint. We concatenated the two chains, with the appropriate statistical weights. Each chain's posterior pdf was multiplied by its own Bayesian evidence $\mathcal{Z} = \int \mathcal{L}(m)\pi(m)dm$ and divided by the sum of both evidences to normalize the resulting pdf to unity,

$$p(m|d)_{\text{tot}} = p(m|d)_{\mu<0} \times \frac{\mathcal{Z}_{\mu<0}}{\mathcal{Z}_{\mu<0} + \mathcal{Z}_{\mu>0}} + p(m|d)_{\mu>0} \times \frac{\mathcal{Z}_{\mu>0}}{\mathcal{Z}_{\mu<0} + \mathcal{Z}_{\mu>0}}. \quad (18)$$

In Fig. 15 we present the results of our scan in the $(m_\chi, \sigma_p^{\text{SI}})$ plane in the most popular case of positive μ with the $(g-2)_\mu$ constraint in the likelihood (a), and in the case where we combine both positive and negative μ scans done without the $(g-2)_\mu$ constraint in the likelihood (b). Differently from our previous studies of the CMSSM [25,26], we do not include the XENON100 [59] limit in the likelihood function, due to the large theoretical uncertainties which render the impact on CMSSM parameters of the present experimental bounds from DM direct detection considerably weaker than the limits obtained from the LHC.

In Fig. 15(a), the FP/HB region, which is just above the XENON100 90% CL upper bound on σ_p^{SI}, has the potential to be ruled out with the sensitivity planned for future XENON1T detector [59]. We checked that the posterior distribution in the case without the $(g-2)_\mu$ constraint and $\mu > 0$ is similar. With respect to what was observed in our previous studies [25,26], we note that the 68% credible region corresponding to the $\tilde{\tau}$-coannihilation region ($200\ \text{GeV} \lesssim m_\chi \lesssim 400\ \text{GeV}$) has been washed out. On the other hand, the A-resonance region ($m_\chi \gtrsim 400$ GeV and $\sigma_p^{\text{SI}} \lesssim 10^{-9}$ pb) is not likely to be further constrained by the new spin-independent cross section measurements planned for the next year.

However, the μ-combined case shows a very different shape for the posterior, due to the total effective coupling being reduced by negative μ. Hence, the FP/HB region yields a slightly lower σ_p^{SI} than in the $\mu > 0$ case. Figure 15(b) shows that the FP/HB region still remains partially below the XENON100 bound. It can be tested with the future XENON1T sensitivity.

IV. STATISTICAL DISCUSSION

We dedicate this section to some further statistical considerations. In Sec. IV A we analyze in detail the individual contributions to the minimum χ^2 of our scans, and try to derive some conclusions on the goodness of the global fit of the CMSSM. Note that Bayesian scans are by definition *not* optimized for calculating the best-fit points to the highest accuracy, because their results are dependent on the choice of priors, while the best-fit point is entirely determined by the likelihood function. Nevertheless, we think that the conclusions presented in this section are general, as they are based on the properties of our likelihood functions over a broad range of parameters. In Sec. IV B we perform a Bayesian model comparison of the model with $\mu > 0$ and $\mu < 0$, based on the relative evidence. We find that both the frequentist and Bayesian approaches favor the case of $\mu < 0$ and without the $(g-2)_\mu$ constraint.

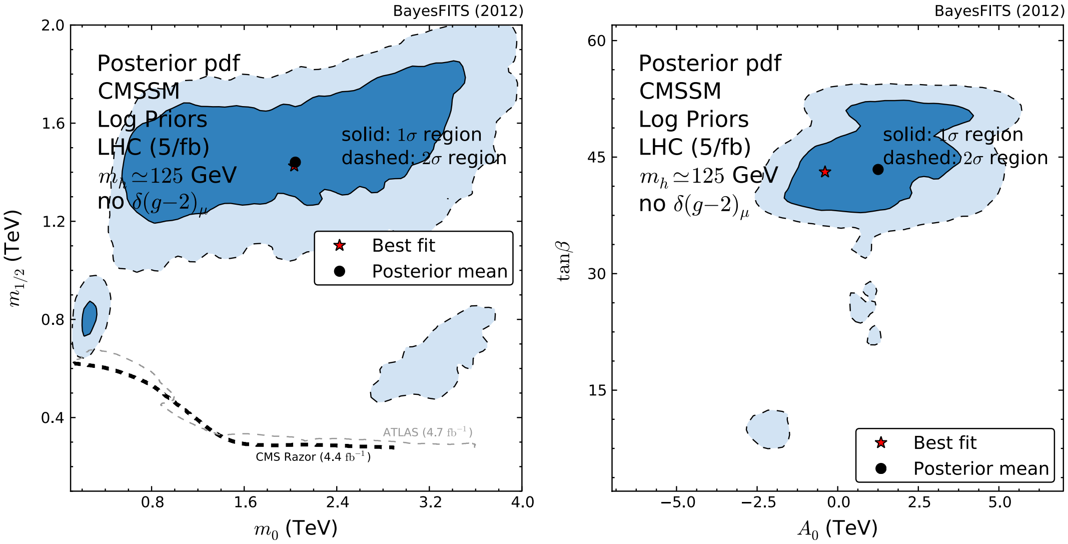

(a) (b)

FIG. 14 (color online). Marginalized posterior pdf in (a) the $(m_0, m_{1/2})$ plane and (b) the $(A_0, \tan\beta)$ plane of the CMSSM for $\mu > 0$ and $\mu < 0$ combined, constrained by the experiments listed in Table III except $(g-2)_\mu$. The dashed black line shows the CMS razor 95% CL exclusion bound.

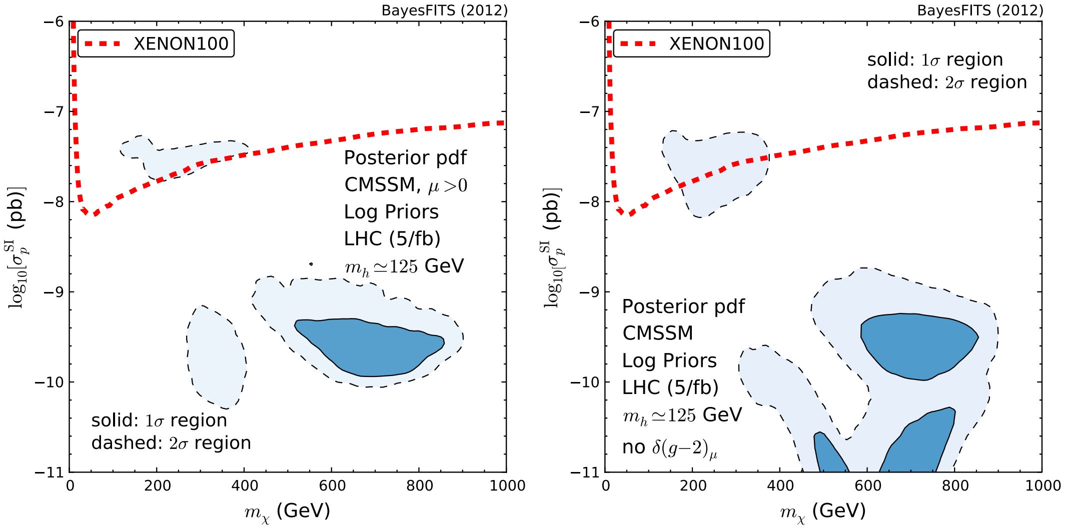

(a)

(b)

FIG. 15 (color online). Marginalized posterior pdf on the (m_χ, σ_p^{SI}) plane in the CMSSM constrained by the experiments listed in Table III, for the case (a) with $(g-2)_\mu$ and positive μ, and (b) without $(g-2)_\mu$ and with a combination of the $\mu>0$ and $\mu<0$.

A. The χ^2 and the best-fit point

In Table IV we present the breakdown of the individual constraint contributions to the total χ^2 of our best-fit points, for the scans performed in this analysis. (We define the test statistic as $\chi^2 = -2\ln\mathcal{L}$) A bar chart showing the main individual contributions to the minimum χ^2 is given in Fig. 16. In Table V we present the best-fit points' CMSSM parameters and the corresponding Higgs mass. As one could have expected, the largest contribution is due to the $(g-2)_\mu$ constraint which is very poorly fitted in the CMSSM after the low-mass region has been excluded by the increasingly constraining LHC limits.

We refrain from calulating p-values for our best-fit points in this paper, given the highly non-Gaussian nature of the distribution of the uncertainties. Nonetheless, we point out that, given the number of constraints we employ, $\chi^2_{\rm min} \simeq 15$–16 seem to indicate that the present status of the global fit to all the constraints, especially $(g-2)_\mu$, is poor.

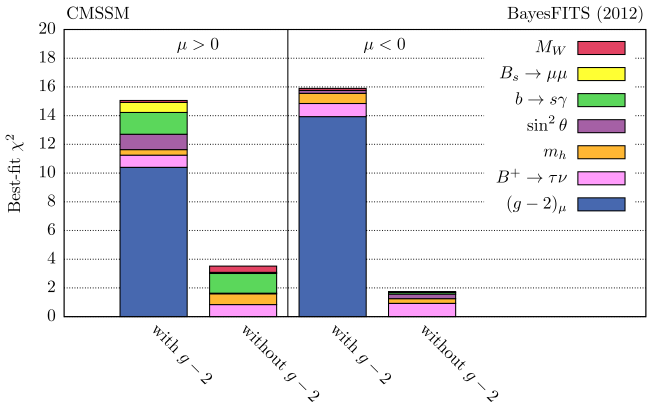

FIG. 16 (color online). A bar chart showing the breakdown of the main contributions to the χ^2 of the best-fit points of our four different likelihood scans.

One important issue should be emphasized when trying to find the position of the best-fit point in a global fit to the CMSSM. At present none of the experimental constraints, including positive measurements of the Higgs mass and the DM relic density, have a strongly constraining effect on the CMSSM parameters. As a result, fairly similar values of $\chi^2 - \chi^2_{\rm min}$ can be achieved over large ranges of the model's parameters. To illustrate the point we show in Fig. 17(a) the combined distribution of the total χ^2, as a function of m_0, for the points that lie along two narrow strips of the $(m_0, m_{1/2})$ plane, with $\mu>0$ and $\delta(g-2)_\mu^{\rm SUSY}$ taken into account. The first strip cuts through the $\tilde{\tau}$-coannihilation region to reach the best-fit point in the A-funnel region. It is parametrized by $m_{1/2} = 1.15m_0 + 485$ GeV, and the points lying along the strip are indicated in blue. The second strip also crosses the $\tilde{\tau}$-coannihilation region with a different inclination, so to reach the A-funnel region at large m_0. It is parametrized by $m_{1/2} = 0.38m_0 + 562$ GeV, and the relative points are shown in red. Both lines cross the 1σ credibility intervals in the $\tilde{\tau}$-coannihilation region and the A-resonance region. The χ^2 distribution shows a plateau that extends across the A-resonance region, with approximately the same χ^2 values as those obtained in the $\tilde{\tau}$-coannihilation region. Thus χ^2 analyses can be very sensitive to minor changes in the adopted methodology (scanning procedure, modeling of the likelihood for different observables, etc.) and, as a consequence, the position of the best-fit point can also undergo dramatic changes. This should be kept in mind when comparing results of different groups.

TABLE V. CMSSM parameters and Higgs masses for the best-fit points of our four different likelihood scans. Masses and A_0 are in GeV.

	m_0	$m_{1/2}$	A_0	$\tan\beta$	m_h	$\chi^2_{\rm min}$
with $(g-2)_\mu$, $\mu > 0$	945	1570	817	45.6	123.3	15.42
with $(g-2)_\mu$, $\mu < 0$	2430	1480	1413	43.7	122.6	16.56
w/o $(g-2)_\mu$, $\mu > 0$	3245	1808	1485	49.2	122.6	3.97
w/o $(g-2)_\mu$, $\mu < 0$	2032	1425	-393	43.1	123.4	2.74

Nevertheless, some general conclusions can be drawn by briefly analyzing the main individual contributions to the best-fit point. For $\mu > 0$, a tension between the Higgs mass at 125 GeV and $(g-2)_\mu$ is expected, as is predicted theoretically by the fact that $M_{\rm SUSY}$ should be large enough to obtain the correct mass of the Higgs, but small enough to fit the $(g-2)_\mu$ constraint. So, naively one would expect that if the latter were released, m_h would show a better fit in the A-funnel region. This is not the case for some parts of the A-funnel region, particularly the one where the best-fit point is located. As Table IV shows, even in the presence of the $(g-2)_\mu$ constraint the contribution of the Higgs to the fit is relatively good.

As we discussed in Sec. III, lifting the $(g-2)_\mu$ constraint allows a better fit to the b-physics observables, which can be seen, particularly in the case of BR($B_s \to \mu^+\mu^-$), by comparing the first and third rows in Table IV. However, even when we keep $(g-2)_\mu$ in place, an even better fit to b-physics can be obtained for $\mu < 0$. Since the SUSY contribution to $\delta(g-2)_\mu^{\rm SUSY}$ is proportional to μ, it becomes negative when $\mu < 0$, and in that case high supersymmetric masses are required in order to suppress it. As we mentioned in Sec. III, for $\mu < 0$ heavy SUSY masses are also required to suppress the chargino-stop contribution to BR($\bar{B} \to X_s\gamma$). Thus the $b \to s\gamma$ and $(g-2)_\mu$ constraints add a same-sign *pull* to the minimum χ^2. Moreover, for the negative μ case, the best-fit point shows an excellent fit to BR($B_s \to \mu^+\mu^-$).

Figure 17(b) shows the χ^2 distribution when the $(g-2)_\mu$ constraint is lifted. When neglecting the observable that has been most difficult to fit, one finds a more informative distribution of the χ^2. The scan clearly favors the regions at large mass scales, as described in the previous sections. Unfortunately, those regions will be much more difficult to probe at the LHC and in DM searches.

In conclusion, one can notice a rather striking improvement of the global fits when the $(g-2)_\mu$ constraint is lifted, exemplified by the drop of more than ten units of χ^2 for one less constraint.

B. Comparison between $\mu > 0$ and $\mu < 0$ without $(g-2)_\mu$

In this subsection, we compare the Bayesian evidences given in our scans to see if either the $\mu > 0$ or $\mu < 0$ case is favored by the experiments, according to Bayesian statistics.

In Table VI we show the log-evidence for our four scans. Two of them include the $(g-2)_\mu$ constraint. In this case we expect $\mu > 0$ to be slightly favored, in agreement with what we found for the χ^2 analysis. The other two scans do not include $(g-2)_\mu$.

The Bayesian evidence favors (it is larger for) $\mu > 0$ when we include $(g-2)_\mu$, but favors $\mu < 0$ when we omit the constraint. Without $(g-2)_\mu$, the Bayes factor (or evidence ratio) yields 2.5:1 in favor of the $\mu < 0$ case. This reads "barely worth mentioning" (1:1 to 3:1) on

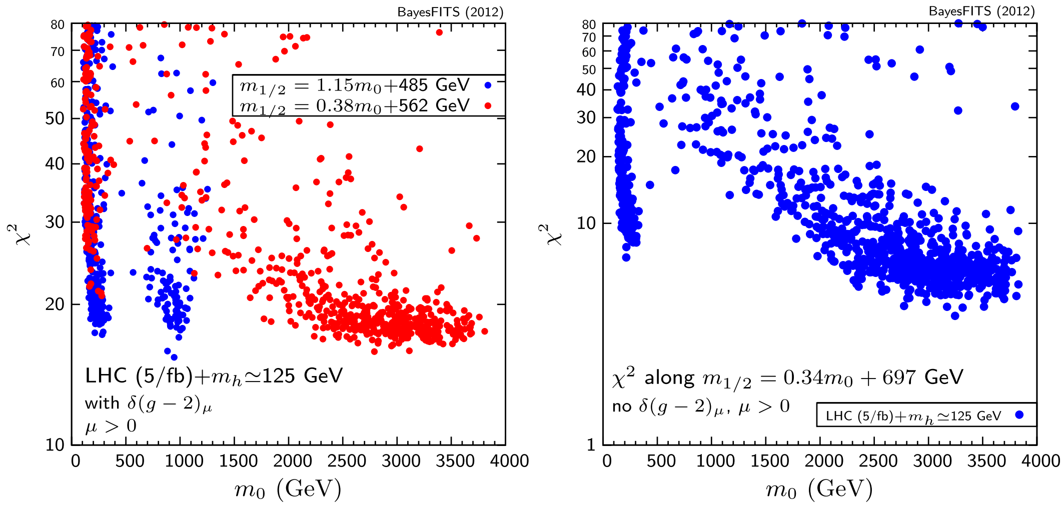

(a)		(b)

FIG. 17 (color online). (a) Scatter plot distribution of the total χ^2 versus m_0 for the points along two narrow strips of the $(m_0, m_{1/2})$ plane parametrized by (in blue) $m_{1/2} = 1.15m_0 + 485$ Gev and (in red) $m_{1/2} = 0.38m_0 + 562$ GeV, with $\mu > 0$, $(g-2)_\mu$. (b) $\mu > 0$, no $(g-2)_\mu$ and $m_h = 125$ GeV. m_0, $m_{1/2}$ parametrized by $m_{1/2} = 0.34m_0 + 697$ GeV.

TABLE VI. Bayesian evidences found for $\mu < 0$ and $\mu > 0$ with and without $(g-2)_\mu$.

	with $(g-2)_\mu$, $\mu > 0$	with $(g-2)_\mu$, $\mu < 0$	w/o $(g-2)_\mu$, $\mu > 0$	w/o $(g-2)_\mu$, $\mu < 0$
$\ln Z$	-18.8	-19.8	-13.5	-12.6

Jeffrey's scale [60], which measures the so-called "strength of evidence." With $(g-2)_\mu$ included, the Bayes factor yields 2.9:1 in favor of the $\mu > 0$ case, which also reads "barely worth mentioning" on the Jeffrey's scale.

We conclude that both the minimum χ^2 and Bayesian approaches indicate that, when the $(g-2)_\mu$ constraint is lifted, the fit for the CMSSM is better for negative μ.

V. SUMMARY AND CONCLUSIONS

In this paper we have performed an updated global statistical analysis of the CMSSM. In terms of new experimental inputs that we incorporated into the likelihood function in an approximate but accurate way, new stringent limits from the CMS razor analysis of 4.4/fb of data on the mass parameters m_0 and $m_{1/2}$, as well as the new limit from LHCb on $\mathrm{BR}(\mathrm{B_s} \to \mu^+\mu^-)$. We also considered the impact of the SM-like light Higgs with mass being close to 125 GeV.

A combination of these new inputs with other usual constraints, most notably from b-physics, electroweak observables and dark matter relic density, as well as from $\delta(g-2)_\mu^{\mathrm{SUSY}}$, generally pushes the favored ranges of posterior probability beyond the 1 TeV scale for $m_{1/2}$ and above ~ 0.8 TeV for m_0, into the A-resonance region where $m_A \sim 2m_\chi$. As for the other two CMSSM parameters: large $\tan\beta$ remains favored, with $\tan\beta \sim 50$, while A_0 remains poorly constrained and can take both signs.

With $\delta(g-2)_\mu^{\mathrm{SUSY}}$ included in the likelihood, the overall fit in terms of χ^2_{min}, for $\mu > 0$, remains poor (compare Table IV; see also e.g., Ref. [25]), invariably primarily due to the high mass scales of the CMSSM causing SUSY to generate only about a tenth of a needed contribution to the variable. This has prompted us to consider the case of negative μ, where we found that χ^2_{min} is not significantly worse.

On the other hand, when we relaxed the $(g-2)_\mu$ constraint (since the CMSSM fails to satisfy it anyway), overall we found a much better fit, with $\mu < 0$ being actually somewhat favored (again compare Table IV). In particular, $\mathrm{BR}(\bar{\mathrm{B}} \to \mathrm{X_s}\gamma)$ is now reproduced much better, as well as $\mathrm{BR}(\mathrm{B_s} \to \mu^+\mu^-)$. This calls for a new serious look at the phenomenology for negative μ.

One concrete observable of interest that is strongly affected by the sign of μ is the spin-independent cross section on DM neutralino σ_p^{SI}. While for both signs of μ its high-probability ranges have now dropped at least an order of magnitude below the XENON100 limit, for negative μ it can become even much lower (compare Fig. 15).

The light Higgs of about 125 GeV remains a challenge for the CMSSM. On the other hand, it is true that physical values of m_h within a or so from 125 GeV can only be achieved at the expense of poor χ^2 [compare Fig. 7(b)] and also for negative A_0.

Finding a stable location of the best-fit point in the CMSSM parameter space is a real challenge because of an extended *plateau* of comparable, low values of χ^2, which we have pointed out for $\mu > 0$ and the $(g-2)_\mu$ constraint included. (Compare also Ref. [25])

In contrast, high posterior probability regions remain relatively robust, but unfortunately now favoring superpartner mass ranges which will be even more difficult to test at the LHC than before, and similarly for DM searches. Thus the CMSSM is now favoring new territories whose experimental exploration may be a real challenge for the next few years.

ACKNOWLEDGMENTS

We would like to thank Maurizio Pierini, Christopher Rogan and Maria Spiropulu for valuable discussions and inputs. E. M. S. would like to thank Azar Mustafayev for discussions on the impact of the $(g-2)_\mu$ constraint. This work has been funded in part by the Welcome Programme of the Foundation for Polish Science. A. J. F. is funded by the Science Technology and Facilities Council. K. K. is also supported in part by the EU and MSHE Grant No. POIG.02.03.00-00-013/09. L. R. is also supported in part by the Polish National Science Centre Grant No. N202 167440, an STFC consortium grant of Lancaster, Manchester and Sheffield Universities and by the EC 6th Framework Programme MRTN-CT-2006-035505.

Note added.—On July 4th, 2012, the discovery at 4.9σ by CMS and at 5.0σ by ATLAS [61] of a boson consistent with the SM Higgs, with mass near 125 GeV, was announced. Particularly, the mass claimed by CMS, $m_h = 125.3 \pm 0.6$ GeV, is very close in central value and experimental error to the signal case considered in this paper. Subsequent to the announcement, we post-processed our chains with a likelihood function modified to incorporate the updated result. We found no changes in the posterior distribution and location of the best-fit point for the putative signal case presented here.

[1] G. L. Kane, C. F. Kolda, L. Roszkowski, and J. D. Wells, Phys. Rev. D **49**, 6173 (1994).
[2] CMS Collaboration, Report No. CMS-PAS-SUS-12-005, CERN, Geneva, 2012.
[3] CMS Collaboration, Report No. CMS-PAS-SUS-11-008, CERN, Geneva, 2011.
[4] S. Chatrchyan *et al.* (CMS Collaboration), Phys. Rev. Lett. **107**, 221804 (2011).
[5] CMS Collaboration, Report No. CMS-PAS-SUS-11-004, CERN, Geneva, 2011.
[6] ATLAS Collaboration, Report No. ATLAS-CONF-2012-033, CERN, Geneva, 2012.
[7] ATLAS Collaboration, Report No. ATLAS-CONF-2012-037, CERN, Geneva, 2012.
[8] CMS Collaboration, Report No. CMS-PAS-HIG-12-008, CERN, Geneva, 2012.
[9] ATLAS Collaboration, Report No. ATLAS-CONF-2012-019, CERN, Geneva, 2012.
[10] G. Aad *et al.* (ATLAS Collaboration), Phys. Rev. Lett. **108**, 111803 (2012).
[11] S. Chatrchyan *et al.* (CMS Collaboration), Phys. Lett. B **710**, 403 (2012).
[12] G. Aad *et al.* (ATLAS Collaboration), Phys. Lett. B **710**, 383 (2012).
[13] S. Chatrchyan *et al.* (CMS Collaboration), Phys. Rev. Lett. **108**, 111804 (2012).
[14] TEVNPH, CDF, and D0 Collaborations, arXiv:1203.3774.
[15] H. Baer, V. Barger, and A. Mustafayev, Phys. Rev. D **85**, 075010 (2012); O. Buchmueller *et al.*, arXiv:1112.3564; M. Kadastik, K. Kannike, A. Racioppi, and M. Raidal, J. High Energy Phys. 05 (2012) 061; J. Cao, Z. Heng, D. Li, and J. M. Yang, Phys. Lett. B **710**, 665 (2012).
[16] H. Baer, V. Barger, and A. Mustafayev, J. High Energy Phys. 05 (2012) 091; S. Akula, B. Altunkaynak, D. Feldman, P. Nath, and G. Peim, Phys. Rev. D **85**, 075001 (2012); L. Aparicio, D. Cerdeno, and L. Ibanez, J. High Energy Phys. 04 (2012) 126.
[17] U. Ellwanger, J. High Energy Phys. 03 (2012) 044; U. Ellwanger and C. Hugonie, arXiv:1203.5048; J. F. Gunion, Y. Jiang, and S. Kraml, Phys. Lett. B **710**, 454 (2012); S. King, M. Muhlleitner, and R. Nevzorov, Nucl. Phys. **B860**, 207 (2012); Z. Kang, J. Li, and T. Li, arXiv:1201.5305; J. Cao, Z. Heng, J. M. Yang, Y. Zhang, and J. Zhu, J. High Energy Phys. 03 (2012) 086; D. A. Vasquez *et al.*, arXiv:1203.3446; E. Gabrielli *et al.*, arXiv:1204.0080.
[18] L. J. Hall, D. Pinner, and J. T. Ruderman, J. High Energy Phys. 04 (2012) 131; T. Li, J. A. Maxin, D. V. Nanopoulos, and J. W. Walker, Phys. Lett. B **710**, 207 (2012); A. Arbey, M. Battaglia, A. Djouadi, F. Mahmoudi, and J. Quevillon, *ibid.* **708**, 162 (2012); A. Arbey, M. Battaglia, and F. Mahmoudi, Eur. Phys. J. C **72**, 1906 (2012); P. Draper, P. Meade, M. Reece, and D. Shih, Phys. Rev. D **85**, 095007 (2012); T. Moroi, R. Sato, and T. T. Yanagida, Phys. Lett. B **709**, 218 (2012); M. Carena, S. Gori, N. R. Shah, and C. E. Wagner, J. High Energy Phys. 03 (2012) 014; A. Arvanitaki and G. Villadoro, *ibid.* 02 (2012) 144; M. Gozdz, arXiv:1201.0875; P. F. Perez, Phys. Lett. B **711**, 353 (2012); C.-F. Chang, K. Cheung, Y.-C. Lin, and T.-C. Yuan, J. High Energy Phys. 06 (2012) 128; N. Desai, B. Mukhopadhyaya, and S. Niyogi, arXiv:1202.5190; L. Maiani, A. Polosa, and V. Riquer, New J. Phys. **14**, 073029 (2012); T. Cheng *et al.*, arXiv:1202.6088; B. Kyae and J.-C. Park, Phys. Rev. D **86**, 031701 (2012); F. Boudjema and G. D. La Rochelle, *ibid.* **86**, 015018 (2012); N. D. Christensen, T. Han, and S. Su, *ibid.* **85**, 115018 (2012); I. Gogoladze, Q. Shafi, and C. S. Un, J. High Energy Phys. 07 (2012) 055; P. Byakti and D. Ghosh, arXiv:1204.0415; M. A. Ajaib, I. Gogoladze, F. Nasir, and Q. Shafi, Phys. Lett. B **713**, 462 (2012); M. Ibe and R. Sato, arXiv:1204.3499; T. Basak and S. Mohanty, arXiv:1204.6592.
[19] S. Matsuzaki and K. Yamawaki, Phys. Rev. D **85**, 095020 (2012); A. Azatov, R. Contino, and J. Galloway, J. High Energy Phys. 04 (2012) 127; G. Blankenburg, J. Ellis, and G. Isidori, Phys. Lett. B **712**, 386 (2012); L. Lopez-Honorez, T. Schwetz, and J. Zupan, arXiv:1203.2064; V. Barger, M. Ishida, and W.-Y. Keung, Phys. Rev. Lett. **108**, 261801 (2012); P. P. Giardino, K. Kannike, M. Raidal, and A. Strumia, J. High Energy Phys. 06 (2012) 117; J. Ellis and T. You, *ibid.* 06 (2012) 140; Y. Bai, P. Draper, and J. Shelton, *ibid.* 07 (2012) 192; P. Draper and D. McKeen, Phys. Rev. D **85**, 115023 (2012); A. Arhrib, R. Benbrik, and C.-H. Chen, arXiv:1205.5536; A. Arhrib, R. Benbrik, and N. Gaur, Phys. Rev. D **85**, 095021 (2012).
[20] C. Balazs *et al.*, arXiv:1205.1568; D. Ghosh, M. Guchait, S. Raychaudhuri, and D. Sengupta, arXiv:1205.2283; J. L. Feng and D. Sanford, arXiv:1205.2372; N. Okada, arXiv:1205.5826; J. L. Feng, Z. Surujon, and H.-B. Yu, Phys. Rev. D **86**, 035003 (2012); B. He, N. Okada, and Q. Shafi, arXiv:1205.4038; A. Barroso, P. Ferreira, R. Santos, and J. P. Silva, Phys. Rev. D **86**, 015022 (2012); L. M. Carpenter and J. Goodman, arXiv:1205.5555; I. Ginzburg, arXiv:1205.5890; J. R. Espinosa, M. Muhlleitner, C. Grojean, and M. Trott, arXiv:1205.6790; K. S. Jeong, Y. Shoji, and M. Yamaguchi, arXiv:1205.2486; I. Donkin and A. K. Knochel, arXiv:1205.5515.
[21] S. Chatrchyan *et al.* (CMS Collaboration), arXiv:1207.7235.
[22] G. Aad *et al.* (ATLAS Collaboration), arXiv:1207.7214.
[23] R. Aaij *et al.* (LHCb Collaboration), Phys. Rev. Lett. **108**, 231801 (2012).
[24] A. J. Buras, Acta Phys. Pol. B **41**, 2487 (2010).
[25] A. Fowlie, A. Kalinowski, M. Kazana, L. Roszkowski, and Y.-L. Tsai, Phys. Rev. D **85**, 075012 (2012).
[26] L. Roszkowski, E. M. Sessolo, and Y.-L. S. Tsai, arXiv:1202.1503; Y. Akrami, P. Scott, J. Edsjö, J. Conrad, and L. Bergström, J. High Energy Phys. 04 (2010) 057; C. Strege, G. Bertone, D. G. Cerdeño, M. Fornasa, R. R. de Austri, and R. Trotta, J. Cosmol. Astropart. Phys. 03 (2012) 030; P. Bechtle *et al.*, J. High Energy Phys. 06 (2012) 098.
[27] O. Buchmueller *et al.*, Eur. Phys. J. C **72**, 1878 (2012).
[28] H. Brown *et al.* (Muon g 2 Collaboration), Phys. Rev. Lett. **86**, 2227 (2001).
[29] M. Davier, A. Hoecker, B. Malaescu, and Z. Zhang, Eur. Phys. J. C **71**, 1515 (2011).
[30] F. Jegerlehner and A. Nyffeler, Phys. Rep. **477**, 1 (2009); M. Davier, A. Hoecker, B. Malaescu, C. Z. Yuan, and Z. Zhang, Eur. Phys. J. C **66**, 1 (2010); K. K. Hagiwara, R. Liao, A. D. Martin, D. Nomura, and T. Teubner, J. Phys. G **38**, 085003 (2011).

[31] F. Jegerlehner and R. Szafron, Eur. Phys. J. C **71**, 1632 (2011).

[32] J. Prades, E. de Rafael, and A. Vainshtein, in *Lepton Dipole Moments*, edited by B.L. Roberts and W.J. Marciano (World Scientific, Singapore, 2010), Vol. 20, 303.

[33] B.C. Allanach, C.G. Lester, and A.M. Weber, J. High Energy Phys. 12 (2006) 065.

[34] L. Roszkowski, R. Ruiz de Austri, and R. Trotta, J. High Energy Phys. 07 (2007) 075; R.R. de Austri, R. Trotta, and L. Roszkowski, *ibid.* 05 (2006) 002.

[35] S. Chatrchyan *et al.* (CMS Collaboration), Phys. Rev. D **85**, 012004 (2012); Reports No. FERMILAB-PUB-11-712-CMS, No. CERN-PH-EP-2011-099, and No. CMS-SUS-10-009.

[36] B. Allanach, Phys. Rev. D **83**, 095019 (2011); P. Bechtle, B. Sarrazin, K. Desch, H. Dreiner, P. Wienemann, M. Krämer, C. Robens, and B. O'Leary, Phys. Rev. D **84**, 011701 (2011).

[37] B. Allanach, Comput. Phys. Commun. **143**, 305 (2002).

[38] A. Djouadi, M. Muhlleitner, and M. Spira, Acta Phys. Pol. B **38**, 635 (2007).

[39] T. Sjostrand, S. Mrenna, and P.Z. Skands, J. High Energy Phys. 05 (2006) 026.

[40] http://physics.ucdavis.edu/~conway/research/software/pgs/pgs4-general.htm.

[41] M. Pierini (private communication).

[42] A. Djouadi, Phys. Rep. **459**, 1 (2008).

[43] L. Roszkowski, R.R. de Austri, and R. Trotta, J. High Energy Phys. 04 (2007) 084.

[44] S. Heinemeyer, O. Stal, and G. Weiglein, Phys. Lett. B **710**, 201 (2012).

[45] http://softsusy.hepforge.org/previous.html.

[46] E. Komatsu *et al.* (WMAP), Astrophys. J. Suppl. Ser. **192**, 18 (2011).

[47] K. Nakamura *et al.* (Particle Data Group), J. Phys. G **37**, 075021 (2010).

[48] J.P. Miller, E. de Rafael, and B.L. Roberts, Rep. Prog. Phys. **70**, 795 (2007).

[49] D. Asner *et al.* (Heavy Flavor Averaging Group), arXiv:1010.1589.

[50] http://mastercode.web.cern.ch/mastercode/.

[51] P. Bechtle, K. Desch, and P. Wienemann, Comput. Phys. Commun. **174**, 47 (2006).

[52] http://www.ft.uam.es/personal/rruiz/superbayes/index.php?page=main.html.

[53] F. Feroz, M. Hobson, and M. Bridges, Mon. Not. R. Astron. Soc. **398**, 1601 (2009).

[54] A. Arbey and F. Mahmoudi, Comput. Phys. Commun. **176**, 367 (2007).

[55] S. Heinemeyer, W. Hollik, and G. Weiglein, Comput. Phys. Commun. **124**, 76 (2000).

[56] G. Belanger, F. Boudjema, A. Pukhov, and A. Semenov, Comput. Phys. Commun. **181**, 1277 (2010).

[57] H. Haber, R. Hempfling, and A. Hoang, Z. Phys. C **75**, 539 (1997).

[58] P.H. Chankowski, J.R. Ellis, and S. Pokorski, Phys. Lett. B **423**, 327 (1998); R. Barbieri and A. Strumia, *ibid.* **433**, 63 (1998); G.L. Kane and S. King, *ibid.* **451**, 113 (1999).

[59] E. Aprile *et al.* (XENON100 Collaboration), Phys. Rev. Lett. **107**, 131302 (2011).

[60] H. Jeffreys, *Theory of Probability* (Oxford University Press, Oxford, 1998).

[61] http://indico.cern.ch/conferenceDisplay.py?confId=197461.